Chapter 4 – FURTHER PARAMETER STUDIES

Here we consider variations on the "canonical cases", whether in kinematics, geometry, testing conditions or other matters that hopefully inform the knowledge-base of the unsteady aerodynamics of pitching, and surging, rotation and translation. In some instances, contributions are ascribed to specific research groups; in others, they are amalgamated into a generic whole.

4.1 RECTILINEAR PITCH AND SURGE NOMINALLY IN TWO DIMENSIONS, AND ASPECT RATIO VARIATIONS IN RECTILINEAR AND ROTATIONAL MOTION

Here the canonical-case kinematics have been retained, but plate AR is varied; a slight exception is the 2B case (rotational surge). No AR study has been conducted for the 2A rotational pitch case. For translational cases, it is useful to distinguish between physical and effective AR. The physical AR is the full span wing of that AR, whereas the effective AR stems from an image (symmetry) plane; elaboration is given below.

4.1.1 Case 1B: Translational Surge

Figure 4-1 compares AR = 2, 4 and 8. The AR = 8 lift history (Stevens) does not vary from the AR = 4 canonical case, but the AR = 2 (Manar) does. The secondary peak in lift at around s/c = 8 is not visible in the AR = 2 case and is especially strong in the AR = 8 case. Evidently this peak is tied to formation and ejection of a secondary LEV – a phenomenon influenced by aspect ratio.
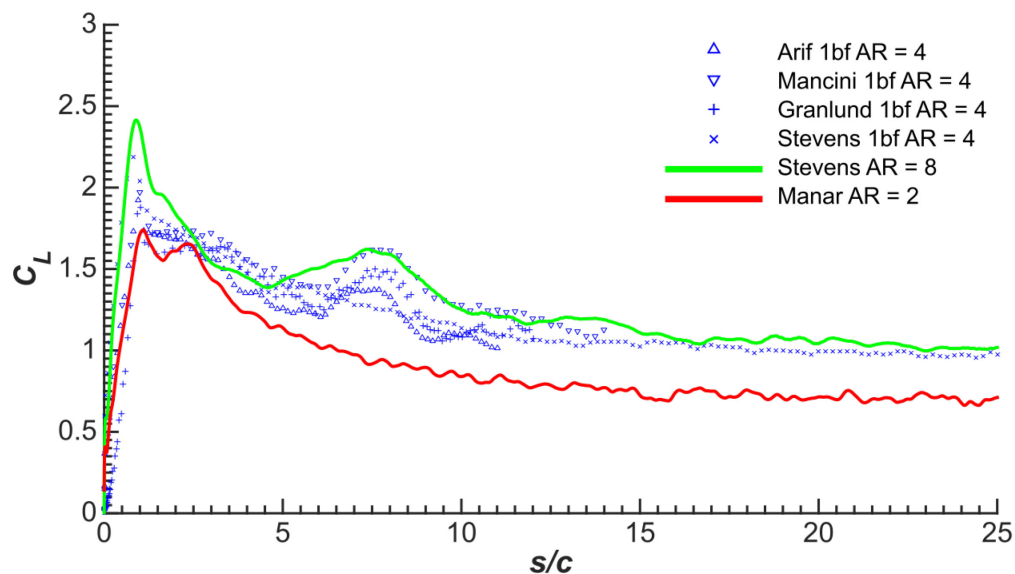

Figure 4-1: Case 1B, Fast Translational Surge AR-Variation.

The slow surge AR-variation lift history is shown in Figure 4-2. Again there is a clear AR effect, with the effective AR = 8 wing producing a higher lift than the corresponding effective AR = 4 data from the same

facility. The AR = 2 data is lower than the higher AR data, but interestingly it is very similar to the effective AR = 4 (physical AR = 2) data of Stevens. This hints that there is an effect of flow three-dimensionality on the lift history and that the use of a symmetry plane may affect the force history. This hypothesis will be discussed further in the following section.
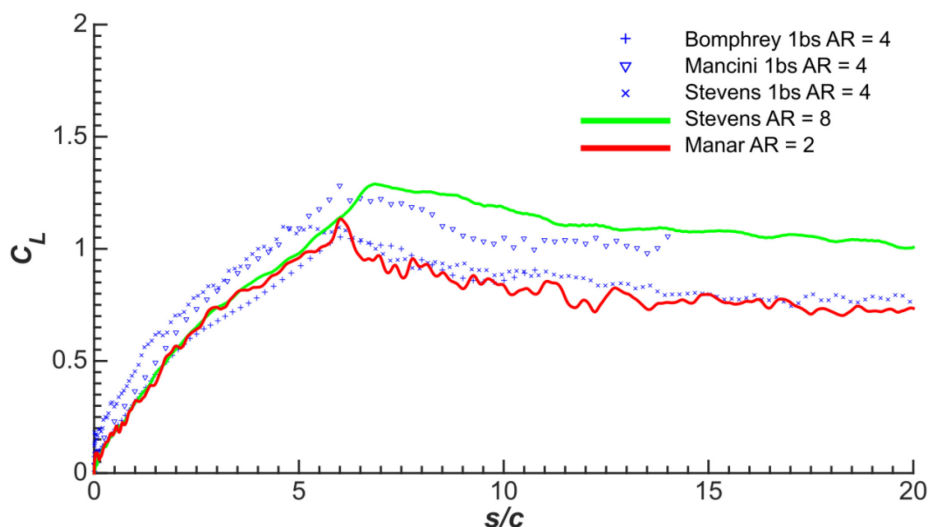

Figure 4-2: Case 1B, Slow Translational Surge AR-Variation.

4.1.2   Case 1A: Translational Pitch

In this section, the effect of force history on AR is complemented by flow visualization.

The fast pitch AR lift history comparison is given in Figure 4-3, and the corresponding slow case in Figure 4-4. The data sets are for plates vertically suspended in water tunnels or towing tanks, and AR-effects include the role of splitter plates. The curves within each figure are qualitatively similar to each other, but there is one key difference. In the region around $s/c = 8$ we see that the secondary rise in the lift is accentuated with increasing AR. When the aspect ratio is increased to 6 and above, a second and even a third bump is present in the force variations.
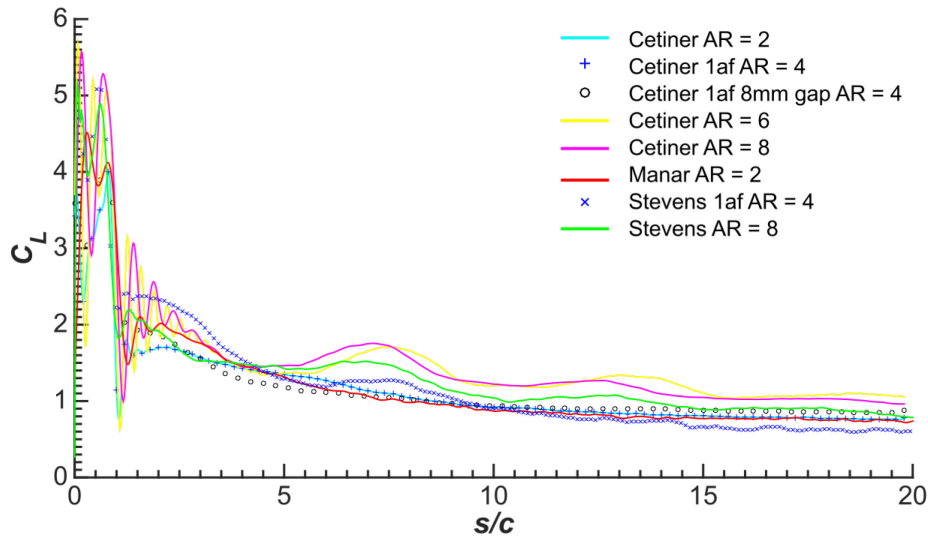
**Figure 4-3: Case 1A, Fast Translational Pitch AR-Variation. All results
are for plates vertically mounted in water tunnels or towing tanks.**
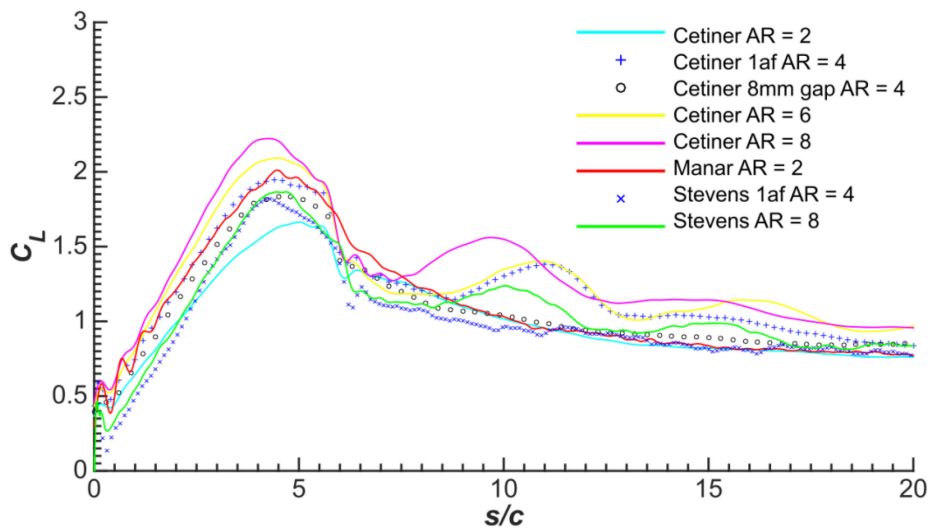

**Figure 4-4: Case 1A, Slow Translational Pitch AR-Variation. All results
are for plates vertically mounted in water tunnels or towing tanks.**

In addition, Cetiner has conducted a series of aspect ratio variation experiments, either using an endplate to represent the symmetry plane or submerging the wing deep in water; this is elaborated in the section on variations of leading edge shape. This includes study of the effect of the gap between the wing and the symmetry plane endplate. When the gap between the root of the wing and the endplate increases to 8 mm, the endplate no longer represents a symmetry plane and the wing behaves as if its effective aspect ratio is equal to its geometric aspect ratio. Therefore a difference in tip vortex formation is incurred. Keeping in mind the difference in the physical span sizes of the wings, the use of a symmetry plane does not create a substantial difference in force

history during the pitching part of the motion, irrespective of the pitch rate. However, the bump in the lift traces differs for the cases where the geometric and effective aspect ratios are equivalent (no symmetry plane cases).

An alternative presentation for the slow translational pitching case, and the fast case, is given in Figure 4-5 and Figure 4-6, respectively. Here we compare three plates mounted horizontally in the test section, with no symmetry plane and no free-surface effects: wall-to-wall plate (nominal 2D case), the canonical AR = 4 (physical aspect ratio) and AR = 2 (also physical aspect ratio). In this presentation, AR-trends are somewhat more apparent than in the prior four figures, especially in lift coefficient; that is, AR-effects on drag are more benign. AR-effects also appear to matter more for the fast case, than for the slow. For the slow case, AR = 2 differs more from AR = 4, than AR = 4 from the nominal 2D case, especially in the sense of the AR = 2 case not evincing a secondary bump in lift at t* ~ 8. Considering the drag variations, the higher-AR producing higher drag is in opposite direction from trends expected from lifting-line theory for induced drag variations with aspect ratio. Clearly, AR-trends are different for attached flow (at 45 degrees incidence) than for separated flow. It remains to ascertain the role of blockage, which is not corrected in any of these results.
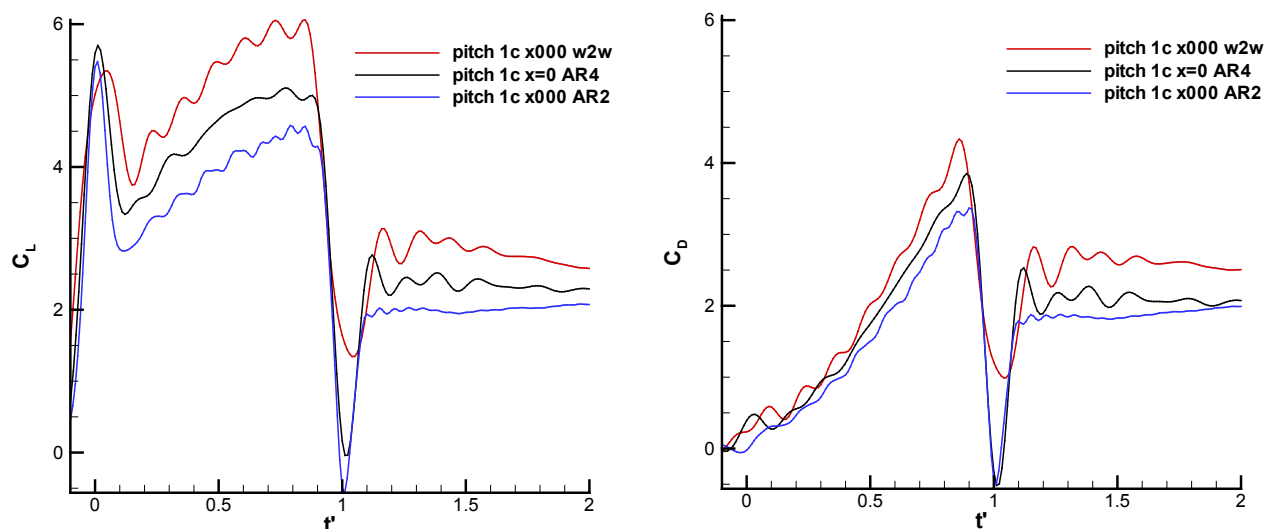

Figure 4-5: Aspect Ratio Effects on 1 *c* (Fast Case) Pitch; Lift (Left) and Drag (Right).
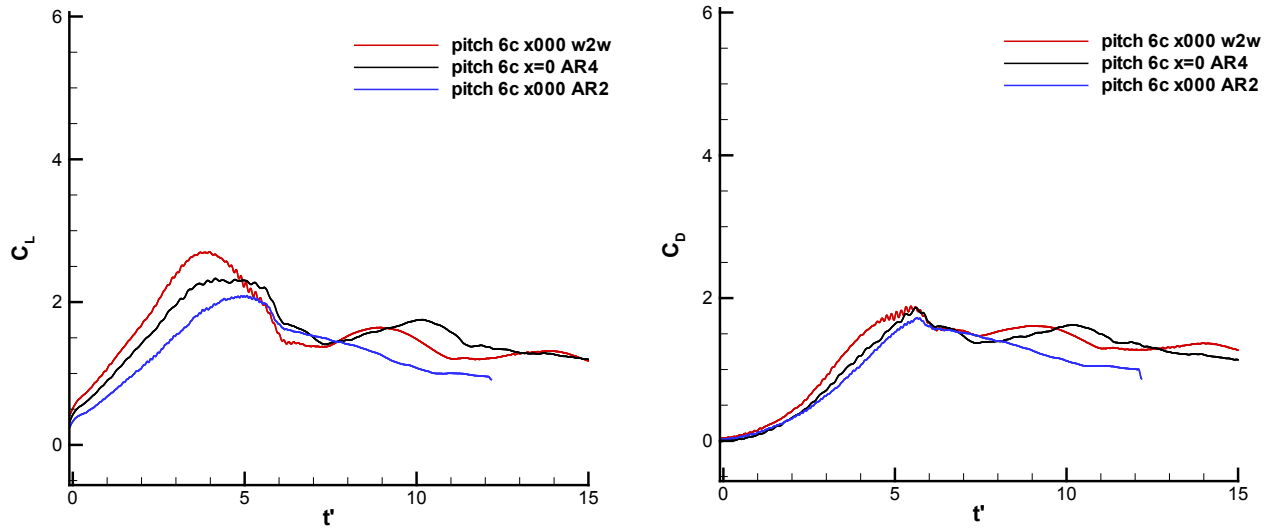
Figure 4-6: Aspect Ratio Effects on 6 *c* (Slow Case) Pitch; Lift (Left) and Drag (Right), 6 *c* Case.

We next turn to flowfield comparisons of aspect ratio effects, examining sectional-images of plates vertically suspended, comparing flow visualization with projected streamlines derived from ensemble-averaged 2D PIV snapshots.

Figure 4-7 covers the fast pitch case, and Figure 4-8 the slow. For both Figure 4-7 and Figure 4-8 the left half of the figure is for effective AR = 4, and the right half for effective AR = 8. Also for both figures, snapshots (a), (c), (e) and (g) show the flow evolution during the pitching part of the motion, while (b), (d), (f) and (h) cover conditions when pitch has completed.
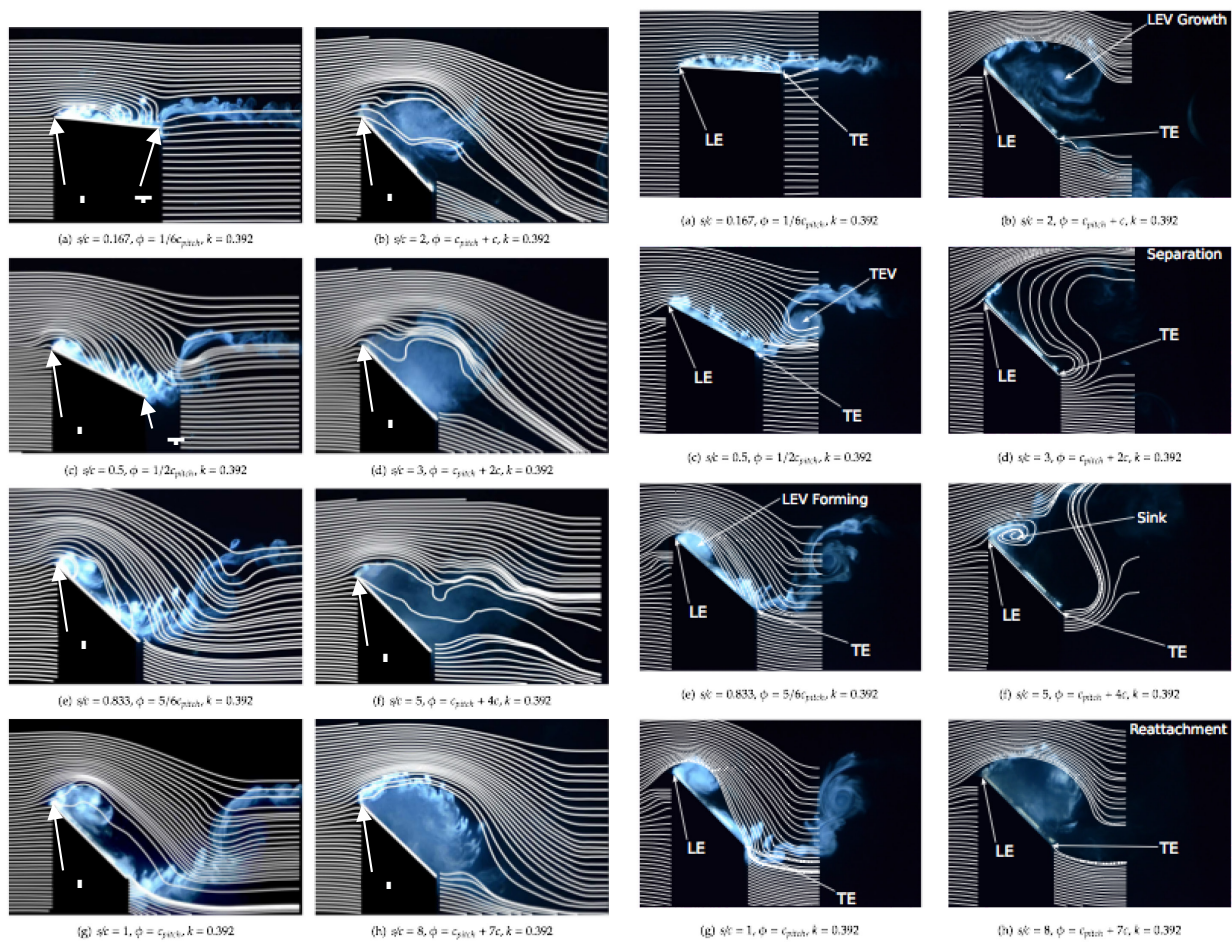
Figure 4-7: Case 1A Fast Pitch, with Pitching Motion Occurring Over One Chord. Flow visualization with PIV ensemble-averaged streamlines superimposed. Effective AR = 4 in left set of eight snapshots, and AR = 8 in right set of eight snapshots.
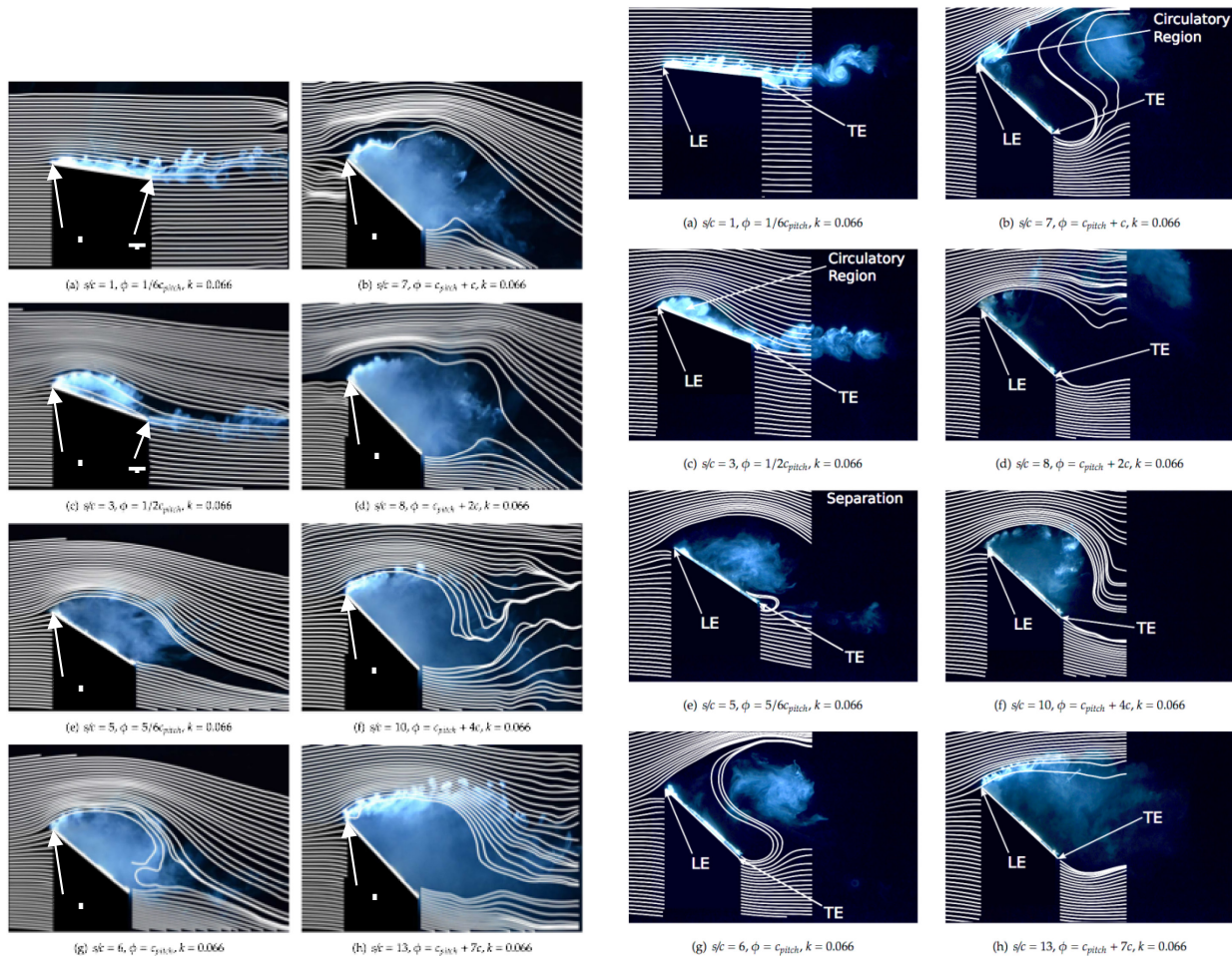
Figure 4-8: Case 1A Slow Pitch, with Pitching Motion Occurring Over Six Chords. Flow visualization with PIV ensemble-averaged streamlines superimposed. Effective AR = 4 in left set of eight snapshots, and AR = 8 in right set of eight snapshots.

Considering first the fast case in Figure 4-7, at $s/c = 0.167$, the dye appears attached to the plate, and there are no signs of flow separation yet. At $s/c = 0.5$, there is a noticeable recirculatory movement of dye in the LE region, suggesting a small LEV. The rest of the flow is attached. Downstream of the TE, a strong vortex (TEV) can be seen. At $s/c = 0.833$, the presence of the LEV is much clearer, and most of the dye is entrained into this flow structure. The TEV has advected aft. At $s/c = 1$, the dye is fully entrained, and a large, coherent LEV is visible, with a clear core region. Streamlines during pitch clearly show bounding of the LEV with highly curved streamlines 're-attaching' before the TE, with the re-attachment point moving aft with increasing incidence. In Figure 4-7(c), we can see that there is an effective camber on the flat-plate, created by the dividing streamline bounding the LEV. This effective camber effect is observed until the end of pitch (where the streamlines begin to lift off). Comparing the effective AR = 4 pitch streamlines with the effective AR = 8 streamlines we observe a very similar pattern, with the exception that the streamlines are more aggressively curved at $s/c = 1$ for AR = 8.

At $s/c = 2$ in Figure 4-7, the LEV continues to grow and the dye disperses, indicating a loss of vortex coherency. Streamline curvature attenuates, and there is no streamline 're-attachment'. At $s/c = 3$, the LEV becomes hard to identify. At $s/c = 5$, a shear layer normal to the plate is seen at the LE. At $s/c = 8$, a large re-circulatory body of

fluid is observed above the wing, lacking the coherency of a LEV, but nevertheless appearing to re-attach at the TE of the plate. Here the streamlines show greater curvature, and the implied pseudo-reattachment correlates directly with the small rise in lift coefficient previously mentioned. Differences between AR = 4 and AR = 8 are somewhat larger after completion of pitching motion, than during the pitch.

The slow-pitch flow visualization in Figure 4-8 again shows that the AR = 8 plate exhibits the secondary lift bump, but at a later convective time (~s/c = 10) than for AR = 4. The lower AR wings typically do not exhibit this feature, suggesting that tip effects are more evident at longer convective times. Unlike for the fast case, there is no indication of the formation of a coherent LEV. There is however a body of flow with a weak circulatory tendency, which is clearly seen at s/c = 3. There is evidence of streamline TE re-attachment up until this point. The flow is broadly separated by s/c = 5. This is in contrast to the fast pitch case, where a dividing streamline reattaches to the plate for the entirety of the pitching motion. Comparison with the pitch part of the cycle for the effective AR = 8 wing shows that for AR = 8, there is a more dramatic loss of streamline curvature than for AR = 4. As regards the secondary bump in lift, again there is a body of circulatory fluid and streamline TE reattachment at s/c = 10 for both the AR = 4 and AR = 8 plates; compare this with analogous reattachment at s/c = 8 for the fast pitch case.

The two-dimensional case is strictly speaking realizable only computationally, as in the wind tunnel or water tunnel there are inevitable endplate effects or wall effects. 2D vortex-particle computations (Figure 4-9; results from the Wroclaw University group) show similarity in LEV and TEV formation relative to the AR = 4 (and other finite-AR) cases during the pitching motion. But after 45-degree incidence has been established, bluff-body shedding in 2D is quite different from that evinced for finite AR, and presumably the absence of tip vortices has implications for both the shedding-history and the lift/drag history.
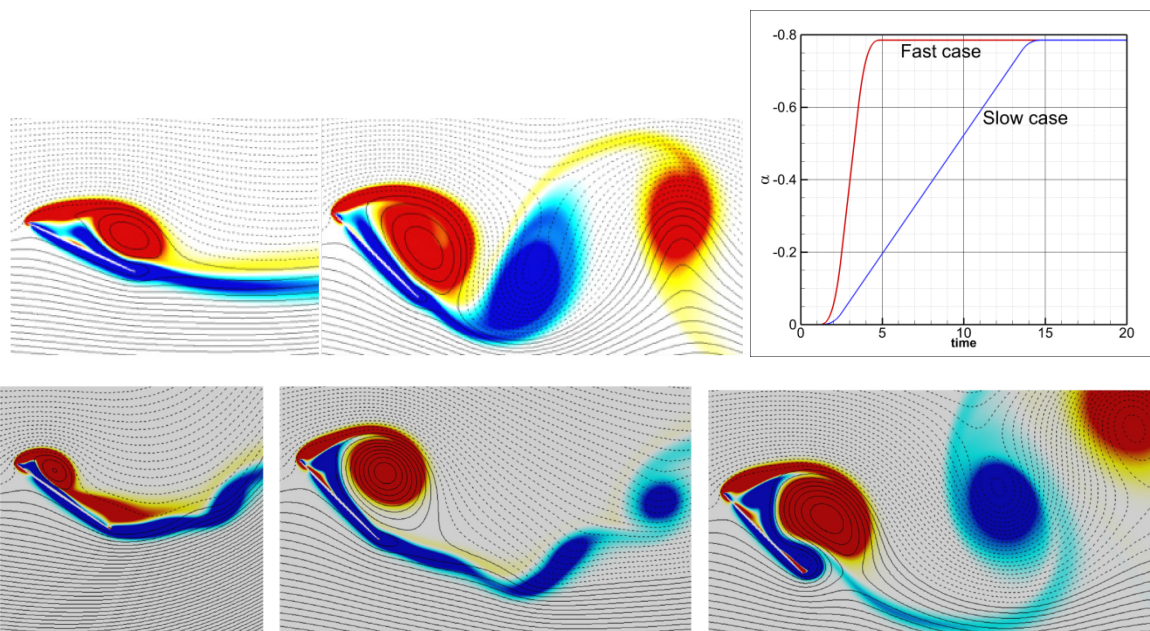

Figure 4-9: Vorticity Contours for Slow Pitch (Top Row) and Fast Pitch (Bottom Row) at the Following Snapshots of Time: for the Slow Case, 8.55, Corresponding to Halfway Up the Pitch Ramp, and 15.58, at the Conclusion of Pitch; for the Fast Case, Time 3.55, Corresponding to Slightly Before Halfway Up the Pitch Ramp, 5.05, at the Conclusion of Pitch, and 10.05, at a Subsequent Vortex Shedding Cycle Well After Motion is Completed. Top right-hand corner: Angle of attack history vs. physical time.

4.1.3 Case 2B: Rotational Surge

The discussion is based on Carr, DeVoria, and Ringuette [40], for plates of AR = 2 and 4. Conditions approximate the fast rotational surge case, 2B. The U_{tip} and span b are used for normalisation, and Re_{span} is matched to isolate AR effects [45].

Figure 4-10 shows a sequence of 3-D Q iso-surfaces versus the angle of rotation, φ, for AR = 2 and 4 plates, Re_{span} = 10,000. The flow structures for AR = 2 and 4 show similarities at $\varphi = 30°$, including outboard LEV lift-off into an arch-like structure, and a perpetually "stable" LEV inboard. These features are in good agreement with Garmann and Visbal [55], Jardin *et al*. [46] and Ozen and Rockwell [19]. As the first LEV lifts off, another forms ahead of it that connects to the TV for both ARs ($\varphi = 30°$). Note also the aft progression of the trailing vortex loop. However, substantial variations with AR exist. The AR = 4 LEV is farther aft at a given percent span than for the shorter AR = 2 wing. For AR = 4, by $\varphi = 60°$ the initial lifted-off outboard LEV is aft of the TE, and three smaller LEVs have formed ahead it. Concurrently, the initial, main TV travels aft of the TE. However, for AR = 2 by $\varphi = 60°$ the first outboard LEV has tilted aft and merged with the TV; both are close to the wing. The AR = 4 outboard LEV becomes larger ($\varphi = 60°$, red arrow), which is a sign of breakdown [47]; this was similarly found by Lu and Shen [48] and Garmann and Visbal [55]. By $\varphi = 90°$, this outboard breakdown has progressed substantially, qualitatively indicated by small, disorganised structures. Breakdown adversely affects the mean-flow convergence from phase averaging, leading to the reduced coherence observed in the iso-Q surfaces. For AR = 2, at $\varphi = 54°$ (inset) the aft-tilted LEV also increases in size. At $\varphi = 90°$, the outboard AR = 2 LEV/TV flow shows prominent breakdown with an LE shear layer ahead of it; the AR = 4 flow exhibits a similar shear layer. The breakdown behavior is similar to the dye flow visualizations of Carr and Ringuette [40]. Despite breakdown, the AR = 2 outboard vortical flow remains more coherent and nearer to the wing.
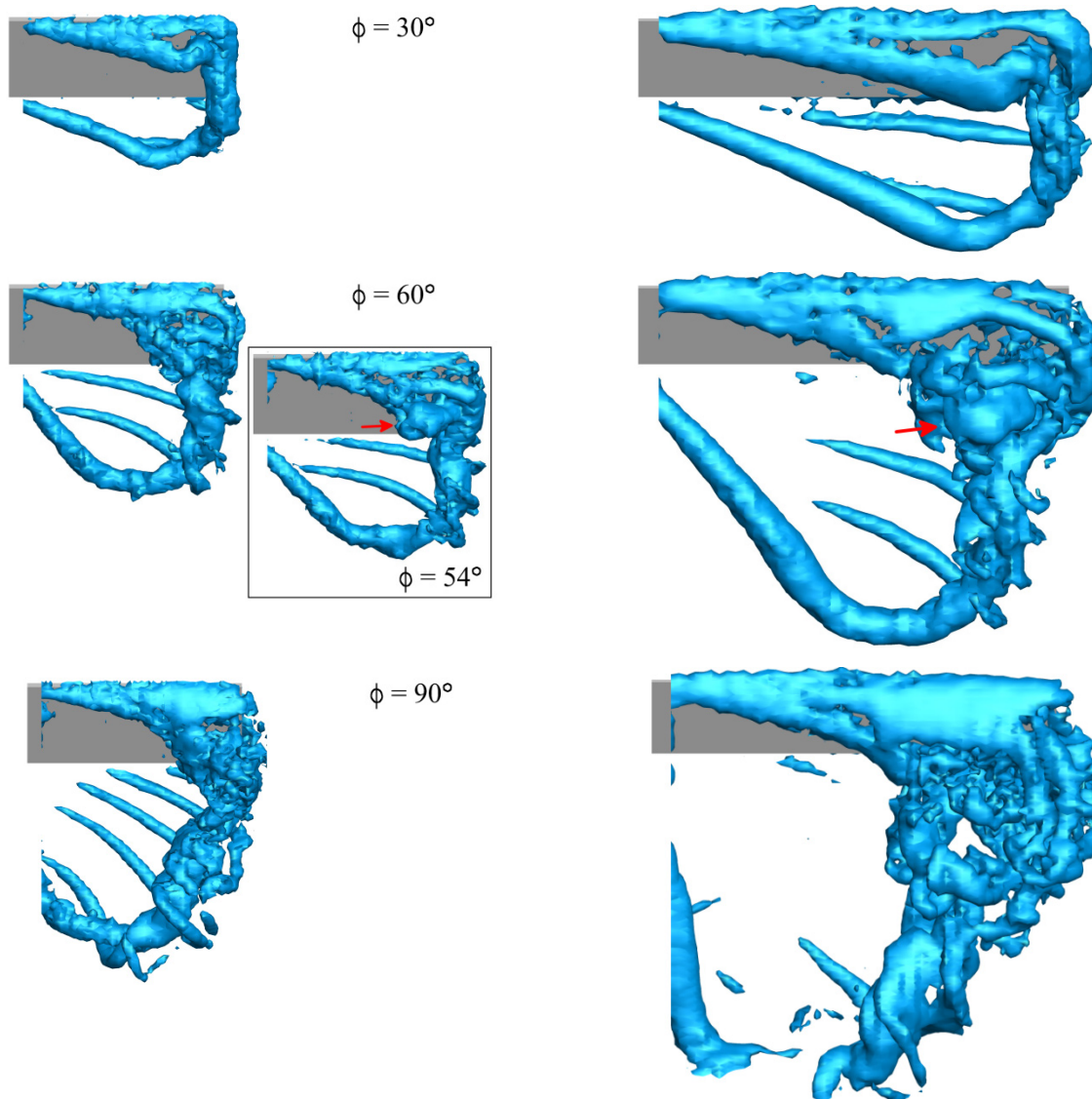
**Figure 4-10: Top, or (*x, z*)-Plane View, of an Iso-Surface of Non-Dimensional
Q = 12 at Various *φ*; AR = 2 (Left Column), AR = 4 (Right Column).
Red arrow indicates LEV enlargement prior to breakdown.**

Figure 4-11 gives span-averaged total and LEV circulations, Γ_{total} and Γ_{LEV}, versus the phase angle of rotation, φ. The Γ_{total} comes from an (*x, y*)-plane ω_z area integral for all grid points with $\omega_z > \omega_{z,th}$ (within a $1\ c \times 1\ c$ domain above the plate for AR = 2, and $1.5\ c \times 1.5\ c$ for AR = 4). It is normalized by the local azimuthal wing velocity, U_{local}, yielding more comparable magnitudes across the span, then averaged from 20% − 80% span. The Γ_{total} increases with φ, with an initially larger slope, and then with a more gradual rise from the continual formation of smaller outboard LEVs. The AR = 2 Γ_{total} is larger, due to its more coherent outboard flow, but the slopes for AR = 2 and 4 are very similar. The Γ_{LEV}, calculated only from identified LEV points, is span-averaged only over the "stable" LEV, from 20% − 60% and 20% − 40% span for AR = 2 and 4, respectively. The AR = 2 Γ_{LEV} grows initially then saturates ($\varphi > 36°$). For AR = 4, after the larger initial slope, Γ_{LEV} increases gradually; fluctuations are from occasional LEV "splitting" at $\sim$ 40% span.
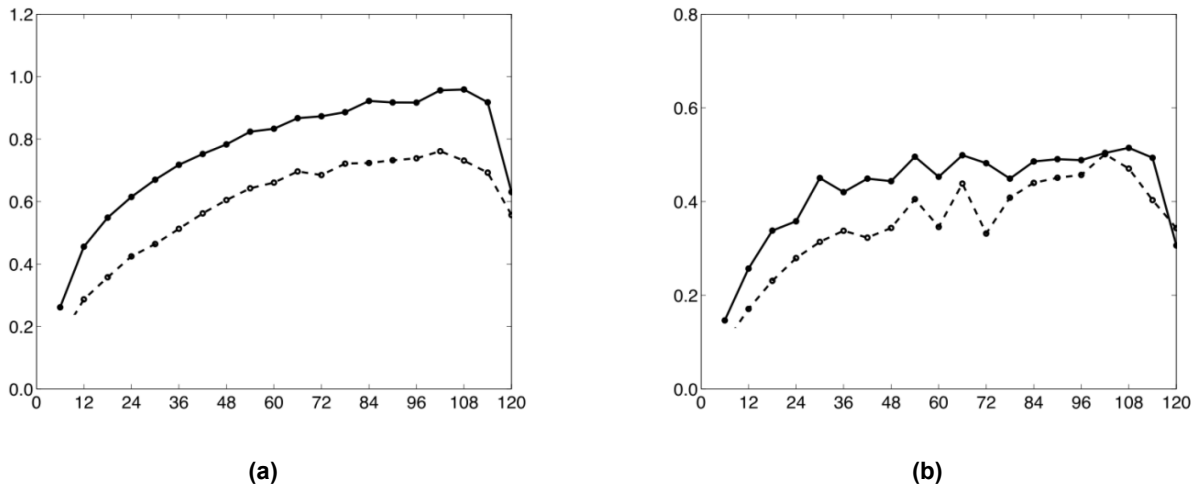
(a)   **(b)**

Figure 4-11: Circulation vs. Phase-Angle of Rotation; (a) Span-Averaged Γ_{total};
(b) Span-Averaged Γ_{LEV}, "Stable" LEV. Solid: AR = 2, dashed: AR = 4.

Figure 4-12 plots C_L (normalized using $U_{75\%}$ for comparison with others) for AR = 1–4 vs. (a) $t^*_{75\%} = tU_{75\%}/c$ and (b) the period for the $\varphi_{final} = 120°$ cases, $t/T_{120°}$. Solid lines indicate $\varphi_{final} = 120°$, while dashed signify 360°; deceleration portions are removed. The $Re_{75\%}$ for AR = 1 – 4 are similar: 4,870, 4,310, 4,120, and 4,030, respectively. Data for $Re_{75\%}$ down to ~ 1,000 show no significant Re effects. Recall that acceleration for all ARs occurs over $\varphi = 10°$, and therefore to achieve a similar $Re_{75\%}$ the lower AR wings require higher acceleration rates, leading to larger initial C_L peaks.

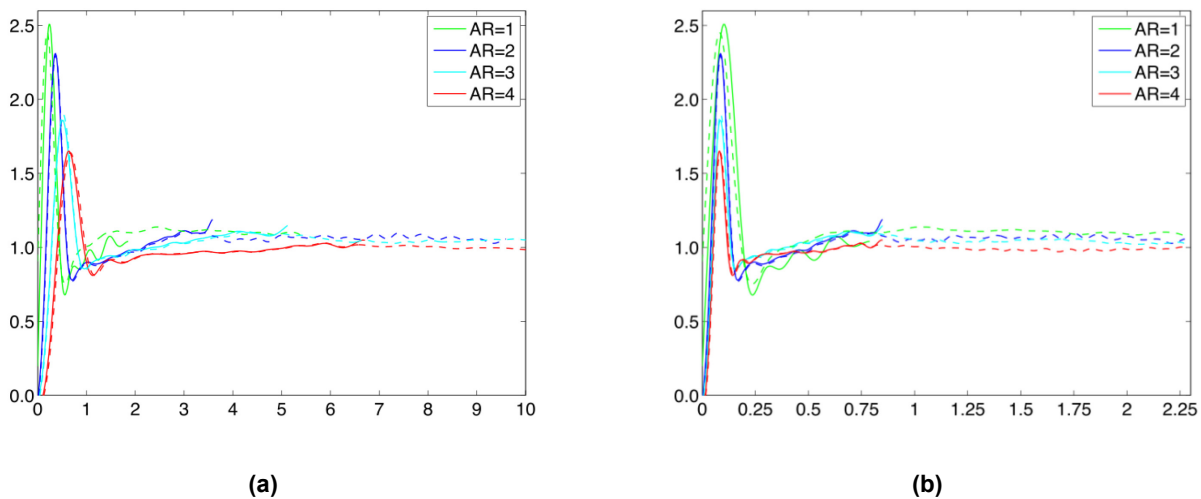
(a)   **(b)**

Figure 4-12: C_L for AR = 1 – 4, (a) vs. t^*, (b) vs. $t/T_{120°}$. Solid: $\varphi_{final} = 120°$, Dashed: $\varphi_{final} = 360°$.
Deceleration portions removed; for (b) not all AR = 4, $\varphi_{final} = 360°$ data shown (see text for details).

Figure 4-12(a) and (b) show common features for all ARs: an initial C_L peak due primarily to non-circulatory force during acceleration, followed by a local minimum, a slow growth period, and finally a plateau; compare with Schlueter et al. [13] When plotted against $t^*_{75\%}$ (Figure 4-12 (a)), the initial peak locations vary with AR, due to the common acceleration over $\varphi = 10°$. When plotted versus $t/T_{120°}$, the C_L peaks essentially coincide.

The slightly higher C_L long-time values for lower AR are likely due to the more coherent TV, which affects a relatively larger portion of the wing. It is a low-pressure region, which will enhance lift, as will its induced upwash near the tip edge [49].

In summary, PIV data indicate a "stable" LEV inboard of ~ 50% span for both AR = 2 and 4, with arch-like LEV lift-off and multiple LEVs outboard. Outboard LEV breakdown is found for both ARs, but the AR = 2 LEV merges with the TV and remains more coherent and near the wing. The slopes of the total spanwise circulation versus rotation angle for each AR are similar, indicating similar LEV force contributions, pointing again to the TV as a main cause for the C_L differences with AR.

4.2   VARIATIONS IN REYNOLDS NUMBER

In this parameter study, the kinematics of the canonical motion is retained, but we compare directly several different Reynolds numbers. Reynolds number was not specified to a "canonical" value, and therefore the experiments and computations mentioned thus far in this Report vary greatly in Re amongst each other. In the present section, the focus is on systematic Re-variations in one test-sequence, thus obviating exogenous effects of different test conditions such as blockage, force-data filtering and so forth.

One scheme for large variations in Reynolds number in the same nominal experimental rig is to mix glycerin and water. Mixtures between 100% glycerin and 100% water yield a kinematic viscosity range of $10^{-6} < \nu < 10^{-3}$ [50] This was the approach taken in the AFRL water tunnel, where a tank with glycerin/water mixture was inserted into the water tunnel test section and surging-type motions using the tunnel's existing linear-motors were run. Since it is impractical to pump glycerin-water mixtures with a conventional axial impeller pump, pitching motions – with a steady free-stream – were not possible. The glycerin/water mixture usage in tanks is not new. Other recent examples include the rotational experiments of Ringuette *et al*. [40].

Figure 4-13 compares lift coefficient history for the "fast" and "slow" translational surge cases at Re = 13 and 29 (pure glycerin), 330 (glycerin-water mix) and 10.000 (pure water).
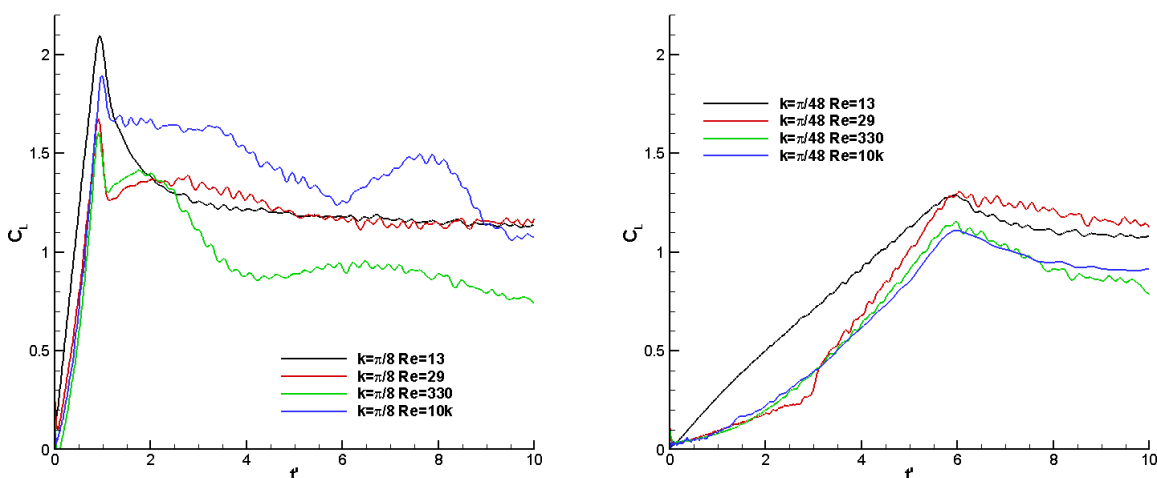

Figure 4-13: Lift Coefficient for an AR = 4 Plate at θ = 45° with Constant Acceleration from Rest, Over 1 Chord (Left) and 6 Chords (Right), to Constant Velocity at Four Different Reynolds Numbers.

In both the fast and slow acceleration motion, the lowest Reynolds number case produces the largest force during the acceleration phase, with all higher-Re cases essentially being the same. The lowest Reynolds number of 13 asymptotically approaches a steady-state value (which would occur after many more lengths than observed here), without any lift fluctuations. This is an indicator of no vortex activity, since there is presumably rapid dissipation of vorticity in the shear layer from the leading edge before it has time to roll up into an LEV. For Re = 29, lift during the constant velocity part is the same as for the lowest Reynolds number. For Re = 330, for the fast case here is a decline in lift after the accelerated-portion is over, relative to the lower-Re cases. For the slow case, this decline persists for Re = 10,000, which is almost identical to the Re = 330 result. For the fast case, the Re = 10,000 evinces higher lift than the very low-Re cases, suggesting that the intermediate value of Re = 330 has some special property. The oscillations in lift during the constant velocity portion of the motion is strongest in the higher-Re case, presumably due to more vigorous LEV and TEV re-formation after the initial starting LEV and TEV once motion first commences. However, in no cases is there a strong trend of lift with Reynolds number. We conclude that the effect of Reynolds number is quite weak, which is perhaps surprising because at the lowest Re there is no discernible LEV or TEV.

For convective problems with a steady free-stream, change in Re generally means changing the test article's size, or the free-stream speed. The former runs into blockage problems if the test article is large, and load-cell signal-to-noise ratio problems in the opposing case of a small test article. The same problem occurs if tunnel free-stream speed is reduced, as small dynamic pressure complicates tares and reduces the load-cell signal. Inversely, a large free-stream speed means a high physical acceleration-rate of the test article, to preserver reduced frequency, and that introduces mechanical vibration and a low (in dimensionless terms) system natural frequency.

Thus in pure water, the available range of Reynolds number is less than one order of magnitude. Figure 4-14 shows the result for the slow translational pitching case for Re from 15 K through 40 K. Over this range, the Re-effect is indeed very small, and perhaps cannot be disentangled from differences in flow quality and load-cell response.
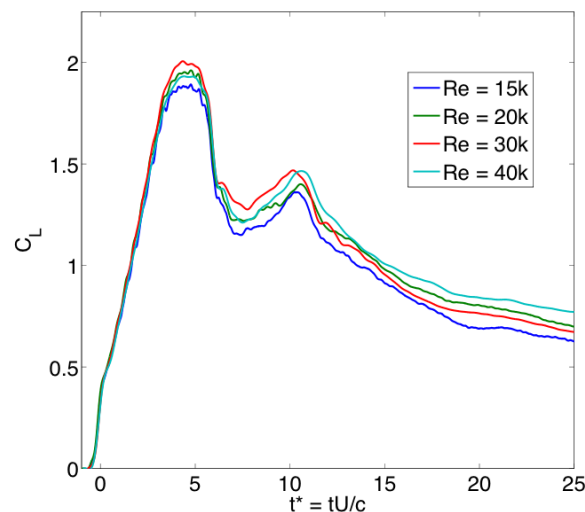

Figure 4-14: AR = 4 Plate Pitching from 0° to 45° in 6 *c* (Slow Case) for Reynolds Numbers 15 K through 40 K, All in Water (No Addition of Glycerin). Re-variation is obtained by changing test-section free stream speed.

The same trend is seen for the flowfield (Figure 4-15) for the fast translational pitching case, this time over nearly an order of magnitude. Flow visualization is possible at very low dynamic pressures, where direct force measurement becomes problematic, and thus the realizable Re-range is broader. In the false-color rendering, four images (all taken at the ¾-span location) of dye injection from the plate LE and TE are superimposed, with color as proxy for Re. One finds close overlap between the four respective LEVs and the four respective TEVs.
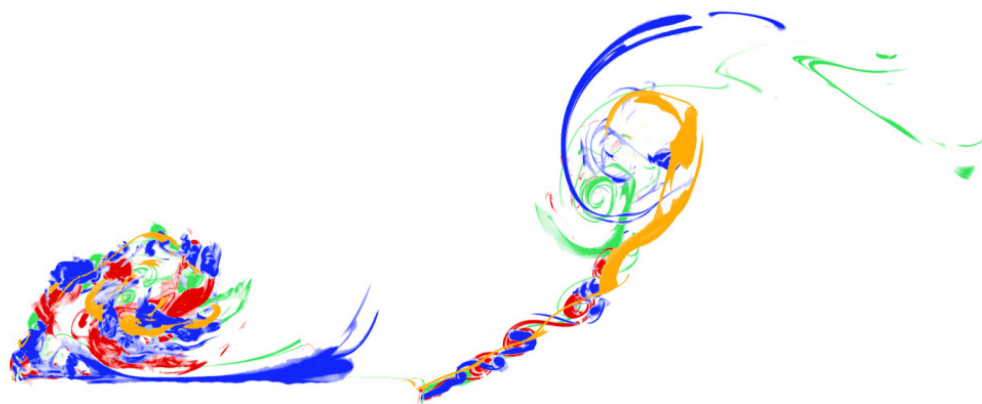
Figure 4-15: False-Coloring of Rhodamine-Dye Planar Laser Fluorescence (that is, Flow Visualization) of the Suction-Side Flowfield of an AR = 4 Plate Pitching from 0° to 45° at Various Re Values, for the "Fast" Case (Pitching Motion Occurs Over One Convective Time; Snapshot is at Completion of One Pitching Motion, by which Time the TEV has Convected ~ 0.7 *c* Downstream of the Plate's TE).

We now turn to rotation vs. translation. Figure 4-16 shows water tunnel measurements on rotational vs. translational fast surge, at a range of Reynolds numbers, for an AR = 2 plate. Except for very low Re (Re = 60 in Figure 4-16), the net aerodynamic force is normal to the plane of the plate, lift and drag histories follow each other closely (so L/D ~ 1 always) and translation appears to have larger aerodynamic force production than rotation, at least at early-time. Note that the non-zero-acceleration portion of the motion in Figure 4-16 occurs over the first convective time; that is, from $t^* = 0$ to $t^* = 1$. It appears to be the case that for the common choice of θ = 45° incidence angle, the peak L/D remains in the vicinity of 1, regardless of motion rate, for Re >1000 and above.
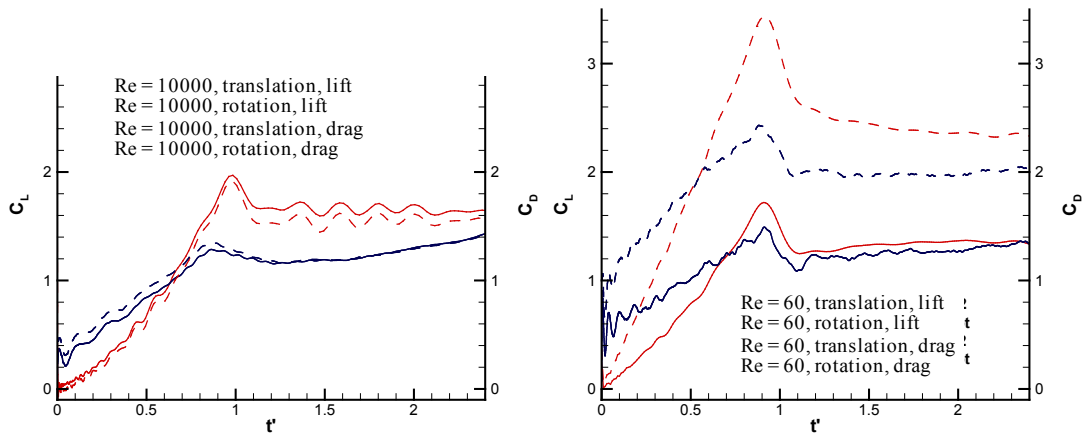
Figure 4-16: Lift Coefficient (Left Ordinate Axis) and Drag Coefficient (Right Ordinate Axis) vs. Convective Time; Lift Coefficient in Solid Lines, Drag Coefficient in Dashed Lines. Translational surge (red), is shown in comparison with rotational surge (black). Left-side plot: Re = 10,000 based on attained steady speed after acceleration concludes; Right-side plot: Re = 60, obtained in mixture of glycerin and water. Lift differs little between Re = 10,000 (left) and 60 (right), while drag at Re = 60 is considerably higher, because skin friction turns the net aerodynamic force aft of wall-normal.

A more comprehensive assessment of Re-effects for fast rotational surge, this time not limited to the early portion of the motion, is shown in Figure 4-17. Here the Re = 120 case (the lowest Reynolds number considered) is something of an outlier, with lower lift than higher values – but between Re = 500 and Re = 10,000 there is little variation.
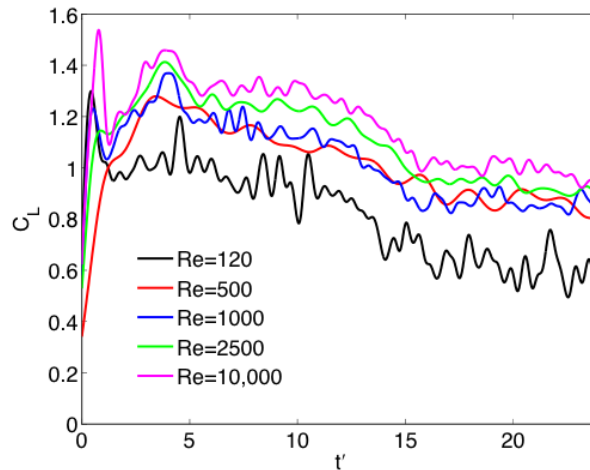

Figure 4-17: Lift Coefficient for a Rotating AR = 2 Plate for a Two Orders of Magnitude Change in Reynolds Number.

We therefore conclude that once Reynolds number reaches a threshold of several hundred, the lift coefficient becomes Re-independent. Drag is somewhat less Re-independent because of the role of skin friction and its

decline with increasing Re. Below this threshold there is some lift variation with Re, depending on the experiment, the style of data-filtering and so forth.

4.3   VARIATION OF REDUCED FREQUENCY

Here we consider the rectilinear (translational) cases, surge and pitch, with the AR = 4 plate. Rotational cases are omitted.

4.3.1   Translational Surge

Variations on the translational surge case, all with 45-degree incidence but with surge acceleration occurring over a duration from 0.25 c through 6 c, are shown in Figure 4-18. Reynolds number is 20,000 in all cases, and all relative free-stream speed-profiles are smoothed linear ramps.
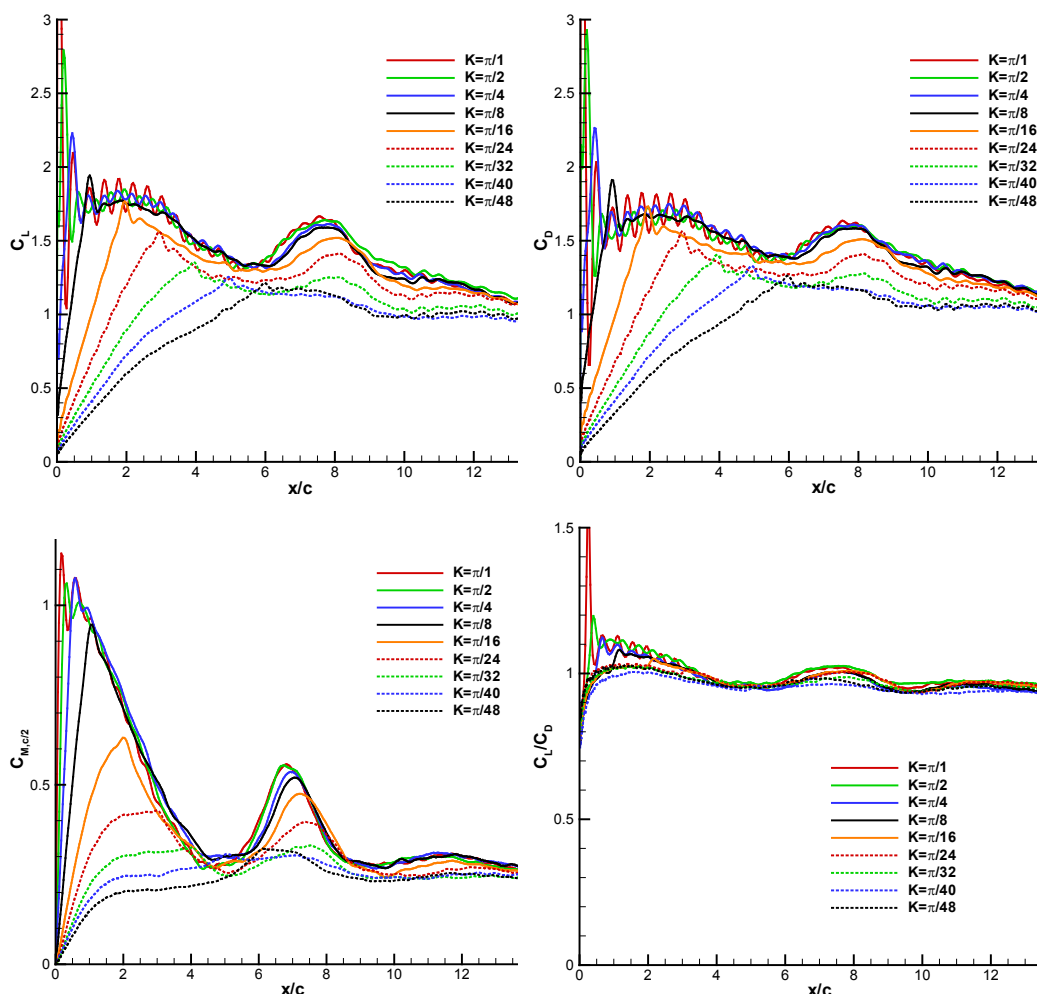

Figure 4-18: Lift Coefficient (Top Left), Drag Coefficient (Top Right), Pitching Moment Coefficient About the Mid-Chord Reference Point (Bottom Left) and Finally Lift to Drag Ratio (Bottom Right) as Functions of Chords Traveled, with Smoothed Linear Ramp of Acceleration from Rest to a Constant Velocity at Re = 20 K, Over Lengths from 0.25 *c* to 6 *c*. AR = 4 rectangular flat plate.

Aside from ramp corner non-circulatory load spikes, and greater apparent oscillations at the highest reduced frequency (where filtering of vibrations will remove the desired frequency content of the actual aerodynamic signal) there is no difference in lift progression when accelerating faster than 1 *c* (K = π/8); all curves of 1 *c* or faster collapse atop of each other. For all accelerations, the history of lift (or drag) with respect to chords-traveled is roughly linear while acceleration is non-zero, and once full surging speed is established there is a plateau or a slight decline in lift. This plateau is at CL = 1.75 for 1 *c* acceleration and above, and progressively smaller for slower surge acceleration. In later time, left declines to a local minimum at 6 *c* travel, where all curves smoothly increase again until a local maximum at ~ 8 *c*, and finally gradually diminish again. When accelerating slower than 1 *c*, a lower maximum lift is achieved, and the local second maximum is attenuated. For all cases, it takes at least 14 chords of travel (beyond the data availability in Figure 4-18) for the various surging acceleration cases to converge towards the same lift value, which is to say to relax to the "steady" (or bluff-body) state. Drag follows lift closely, except for the initial lift-spike at time ~ 0+, as indeed L/D ~ 1 for all other times. Pitching moment coefficient (taken about the mid-chord) follows an undulating history qualitatively resembling that of lift.

4.3.2   Translational Pitch

Here again the peak incidence is 45 degrees. As with all pitch-cases reported here, the starting angle of incidence is zero. Pivot point is the leading edge. Re = 20,000, as in the foregoing section. Besides the two canonical cases ("fast" and "slow"), which are plotted together, we introduce a third case, where the pitch-ramp occurs over two convective times (Figure 4-19). Peak lift declines monotonically with progressively lower pitch rate, as stands to reason, given the respective attenuation in pitch-rate-induced lift. Figure 4-19 also plots lift history vs. a time-base normalized by the pitch rate, so that all motions begin at zero and end at the same value of time. Such overlay shows that the increase in lift due to pitch-rate indeed goes to zero once the motion is completed. The intermediate value of pitch rate also evinces an intermediate value of non-circulatory "bump" associated with the pitch-acceleration start-up transient. This is quite prominent in the fast-case, and absent in the slow one. Looking at the longer-term lift or drag history, it is evident that all cases mutually converge by about 6 – 8 convective time, yet even then the lift (or drag) value is ~ 1.5, which is far above the steady-state or bluff body value.
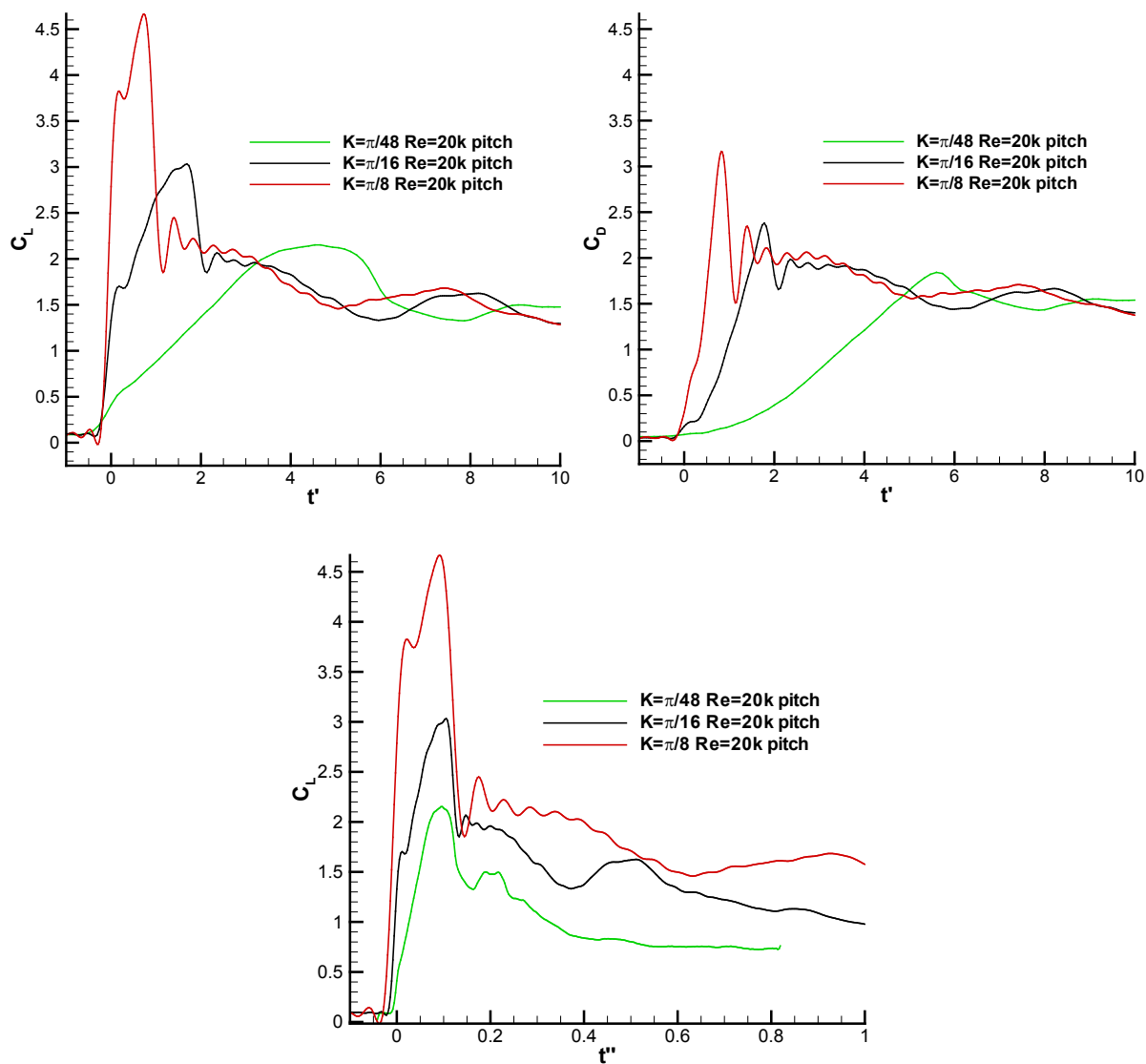
Figure 4-19: Lift and Drag Coefficient Histories for AR = 4 Rectangular Flat Plate at Fast, Intermediate and Slow Pitch Rates; Pivot at Leading Edge, Re = 20 K. Bottom row: Lift coefficient history rescaled by pitch rate.

4.4 VARIATION OF PITCH PIVOT POINT ALONG THE PLATE'S CHORD

In most of this Report, we limit the pitching cases to the leading edge pivot point. In the present section we take five different pivot point locations: x/c = 0, 0.25, 0.5, 0.75 and 1.0. Figure 4-20 presents the 1 c case, while Figure 4-21 presents the 6 *c* case. Clearly, pivot point effects are much stronger for the faster pitch rate. The differences in lift are more profound than in drag. Differences in circulatory lift are primarily a steady offset and not a slope change, and are ascribable to the "Magnus effect".
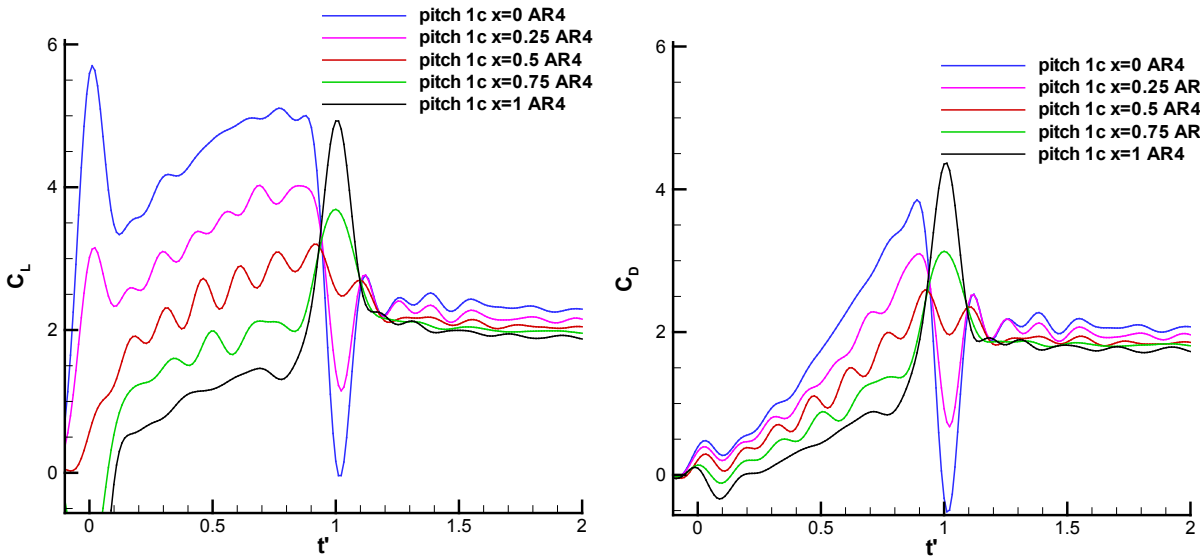
Figure 4-20: Pivot-Point Effects for Pure-Pitch Cases, 1 *c* Motion, AR = 2 (Top Row), AR = 4 (Middle Row) and Nominally 2D (Bottom Row); Lift (Left Column) and Drag (Right Column). Pivot point at leading edge (x/c = 0), x/c = 0.25, 0.5, 0.75 and 1.0 (trailing edge).
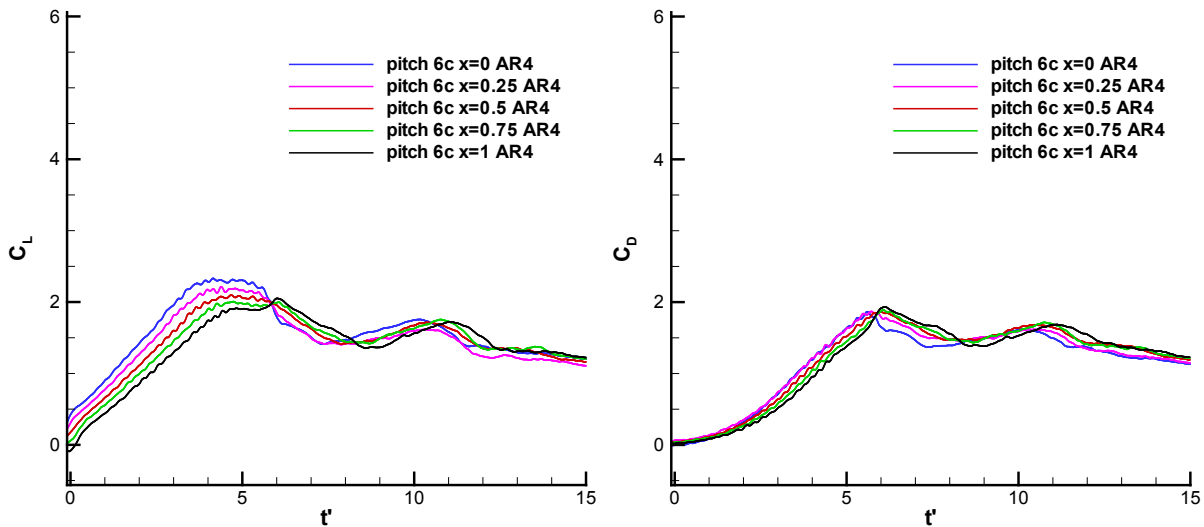

Figure 4-21: Pivot-Point Effects for Pure-Pitch Cases, 6 *c* Motion, AR = 4. Lift (left column) and Drag (right column). Pivot point at leading edge (x/c = 0), x/c = 0.25, 0.5, 0.75 and 1.0 (trailing edge).

For the fast case, differences in non-circulatory lift are quite obvious, and are qualitatively consistent with the implications of the low-order model proposed in this Report. With the pivot point maximally upstream, there is a positive non-circulatory lift spike when pitch-acceleration is positive (early in the motion history), and a negative spike in both lift and drag when pitch-acceleration is negative (t'~ 1). For pitch about the mid-chord, there is no non-circulatory contribution, arguing from symmetry. For pitch about a point downstream of the mid-chord, the sign of the force spike reverses: negative spike in lift when acceleration is positive, positive spike in lift and drag with acceleration is negative.

For the slow case, (Figure 4-21), a more upstream pivot point also produces higher peak lift due to a constant positive offset, but now the acceleration is too slow to produce a demonstrable non-circulatory force contribution in any of the motions. We mention in passing that peak lift for the $x/c = 0$ pivot-case appears to occur when t'~ 4; that is, at a time from motion onset during which the free-stream has traveled approximately 4 chords. The offset between the five lift curves in Figure 4-21 can be regarded as an offset in the abscissa alternatively as an offset in the ordinate. Considering the former, each curve differs from its neighbor by t'~ 0.25 – that is, by approximately the difference in pivot point location. It therefore appears that if the pivot point is taken as an origin, in all cases peak lift is achieved when the free-stream has convected downstream through a distance of 4 chords past the pivot point. One is tempted to wonder whether this is coincidental, or relatable to the oft-quoted conceptualization of a critical "formation number" of 4 [51].

4.5 VARIATIONS IN ACCELERATION PROFILES

Nearly all of the motions studied in this Report are smoothed linear ramps. Smoothing is at the ramp-corners, which is to say at motion initiation and cessation. Here instead we vary the acceleration profile according to an exponential equation. For an analog of the slow translational surge case (6 chords), we have:

$$u(t) = \begin{cases} kt^n & x/c < 6 \\ U_\infty & x/c \geq 6 \end{cases}, \quad k = U_\infty / t_a^n, \quad t_a = (n+1)6c / U_\infty \qquad \text{(Eq. 4-1)}$$

These kinematics are shown in Figure 4-22. For the same acceleration distance, early higher acceleration (fuller velocity profile) produces a higher lift coefficient throughout the acceleration phase. The coefficient *n = 1* recovers the standard case. In Figure 4-23, we instead use a different normalization scheme, where the dimensional lift is normalized by instantaneous dynamic pressure, instead of the dynamic pressure comporting with the steady-state relative free stream. Lift coefficient is initially infinite, since initial velocity is zero. During the first chord of travel, for faster accelerations, lift reduces at a faster rate than for slower accelerations. At s/c = 2, all curves collapse, and lift is now independent of acceleration until s/c ~ 5.5, which nears the end of the acceleration phase. For s/c > 6, all five cases have the same constant velocity and are thus normalized the same way as in Figure 4-22. Initially in the motion, we have a formation of a leading edge vortex, and at some chordwise travel presumably the LEV is considered to be detached. This is where the curves collapse. At s/c ~ 6, a new LEV forms and the curves diverge based on the strength of the 2nd LEV, which in turn is dependent on the strength of the 1st-formed LEV.
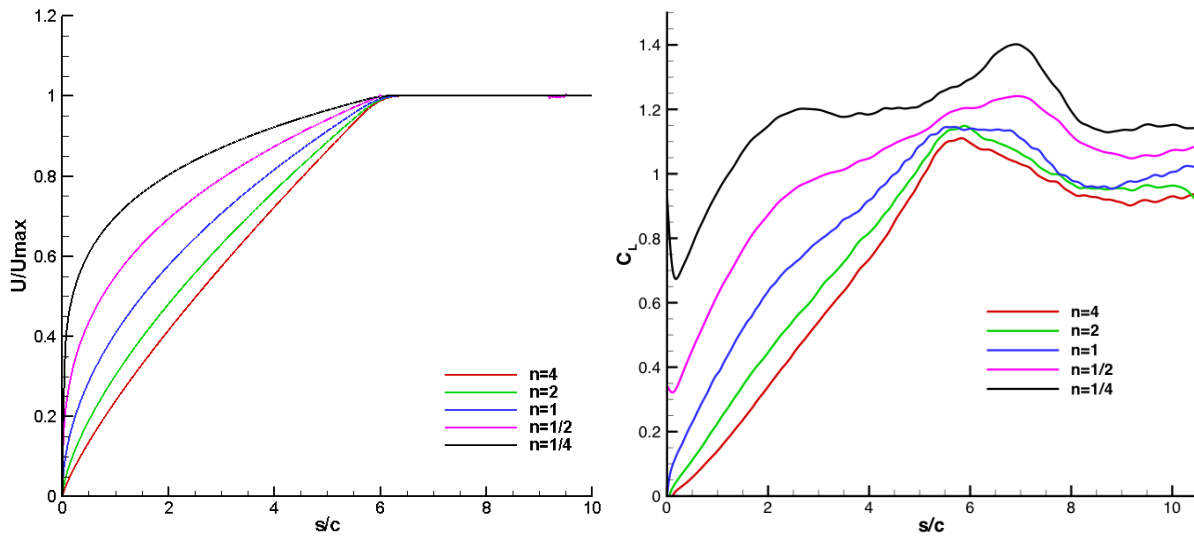
Figure 4-22: Velocity Profiles (Left) and Lift Coefficient (Right) for an AR = 4 Plate at θ = 45° Accelerating Over 6 Chords to Constant Velocity with Five Different Acceleration Profiles.

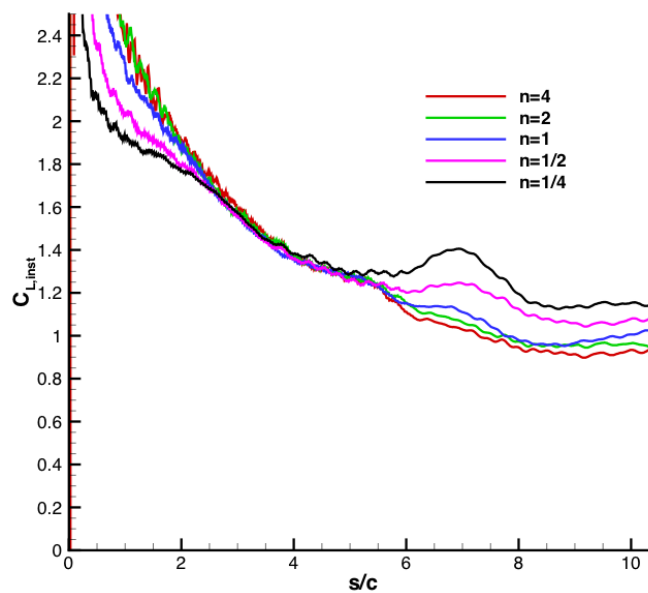**Figure 4-23: Lift Coefficient Normalized by Instantaneous Dynamic Pressure for AR = 4 Plate at θ = 45° Accelerating Over 6 Chords to Constant Velocity with Five Different Acceleration Profiles.**

4.6 VARIATIONS IN TRANSLATIONAL KINEMATIC MODALITY: PLUNGE, SURGE, AND PITCH-SURGE

Here we consider two lines of investigation. The first is based on Kriegseis *et al*. [52], and is concerned with a plunging motion in a steady free-stream, yielding an angle of attack history following that of a pitch-ramp.

Emphasis is on vortex transport. The second topic is comparison of lift and drag history between pitch, surge, plunge, and the combined motion of pitch-surge. All cases are translational.

4.6.1   Vortex Dynamics for Surge vs. Plunge

For the first topic, the question is one of long-term significance of initial conditions. In a surge, the starting-case has zero flow, and obviously there are no boundary layers yet. Boundary layers and the associated vorticity production form after the motion starts. In an "equivalent" (in the quasi-steady sense) plunging motion, there is already an established free-stream, and therefore boundary layers. The motion alters the extant boundary layers and presumably affects the accumulation and ejection of vorticity.

To study the influence of initial conditions, we compare:

1)   Surging (acceleration) of a plate from rest at a constant angle of attack to a final towing speed.

2)   Perturbation of a developed boundary-layer flow on a flat plate with a sudden cross-stream plunging motion superimposed onto a constant free stream velocity.

These two cases will henceforth be referred to as surging and plunging, respectively, as shown in Figure 4-24. In order to contrast these two cases, the two main relevant characteristic velocities – free stream velocity and effective shear-layer velocity – must be considered in the development of vortex circulation.
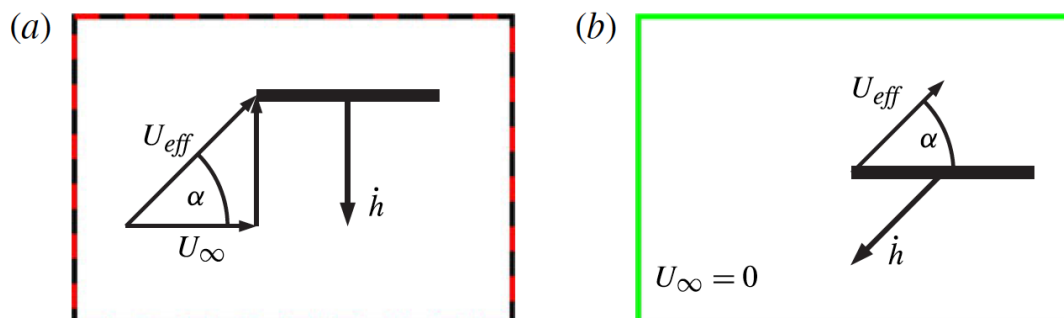

**Figure 4-24: Kinematics Used in this Study. (a) Plunging case(s): Plunge with effective velocity
of 0.1 m/s (P45 0.1, red) and with effective velocity of 0.07 m/s (P45 0.07, black);
(b) Surging case: Surge to 0.1 m/s (T45 0.1, green).**

When examining these characteristic velocities, on the one hand, it is known that the feeding shear layer controls the growth and thus strength of LEVs through the flux vorticity-containing mass into the LEV. Therefore, the advection of circulation into the LEV is a function of the shear layer, with the effective velocity as the only characterizing velocity measure. This suggests that one should define the kinematics of surge and plunge with identical effective shear-layer velocities for proper comparison. On the other hand, one could argue that the characteristic velocity to compare surging and plunging plates is the free stream velocity to ensure an identical bulk Reynolds number for all cases.

Consequently, both characteristic velocities will be considered in the present study in order to clarify this issue. Subsequently, the influence of initial conditions on vortex growth will then be studied for both near-mid-plane and near-tip regions.

LEV circulation histories in the near-mid-plane region for all three test cases are compared in Figure 4-25. In Figure 4-25(a) the non-dimensional circulation and convective time are normalized with the free stream velocity, which corresponds to the final tow speed for the towing case. Owing to the additional boundary-layer vorticity, one would expect a constant offset for the circulation histories between the plunging case P45_0.1 and the towing case T45_0.1, as sketched in Figure 4-25(a). However, the difference between both plunging cases and T45_0.1 shows a larger offset. In order to explore the cause of this larger offset, the free stream velocity is replaced with the effective shear-layer velocity U_{eff} to normalize circulation and time, in Figure 4-25(b). This is particularly sensible since the vortex growth rate is determined by both the generation of vorticity and advection of circulation at the leading edge, each of which is limited by U_{eff}. The non-dimensionalization used in Figure 4-25(b) reveals a collapse for the two plunging cases together (P45_0.1 and P45_0.07) with the towing case T45_0.1. Despite the varying initial conditions between plunging and towing, it must be concluded that the initial boundary-layer vorticity, at least in the near-mid-plane region, plays little role in the vortex formation process. In other words, the initial layer of vorticity must be rapidly annihilated with an opposite-signed layer on the plate surface once the motion begins. Therefore, it has to be concluded that rapid acceleration of fluid boundaries (e.g., moving or morphing obstacles) accelerates fluid with opposite-signed vorticity towards an existing boundary layer, which leads to the sudden cross-annihilation of the two vorticity layers.
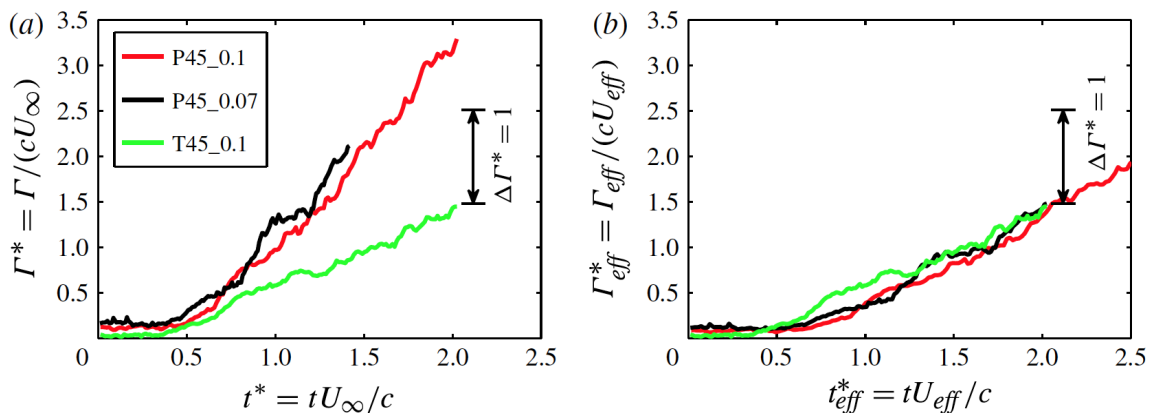

Figure 4-25: Near-Mid-Plane Circulation and Convective Time Normalized with Freestream Velocity (a) and with Effective Velocity from the Shear Layer (b). Note P45_0.1 and P45_0.07 represent two identical plunging cases with differing Reynolds numbers while T45_0.1 is the equivalent surging case.

Both findings – a collapse of circulation and loss of memory of initial conditions – are confirmed by LEV formation plots: Figure 4-26 shows the temporal evolution and corresponding spatial distribution of spanwise vorticity for the near-mid-plane region (**XY**-plane) of all three cases. The iso-lines reveal a similar growth of the LEV for all three cases, which reaffirms the insights obtained from the circulation plots of the near-mid-plane region as shown in Figure 4-26. However, after the acceleration of the plate stops, it can be observed that the tow case LEV starts to roll off the plate. Despite identical circulation, as demonstrated in Figure 4-26, this beginning roll-off might adversely affect the resulting magnitude of the lift force for the towing case. It is important to note that the plate-fixed frame of reference in fact is an accelerated reference frame. As such, the (attached) vortical structures are accelerated according to the orientation of the respective plate kinematics in an inertial system. It is therefore hypothesized that the remaining inertia of the accelerated fluid causes the roll-off of the tow case LEV once the plate acceleration stops.
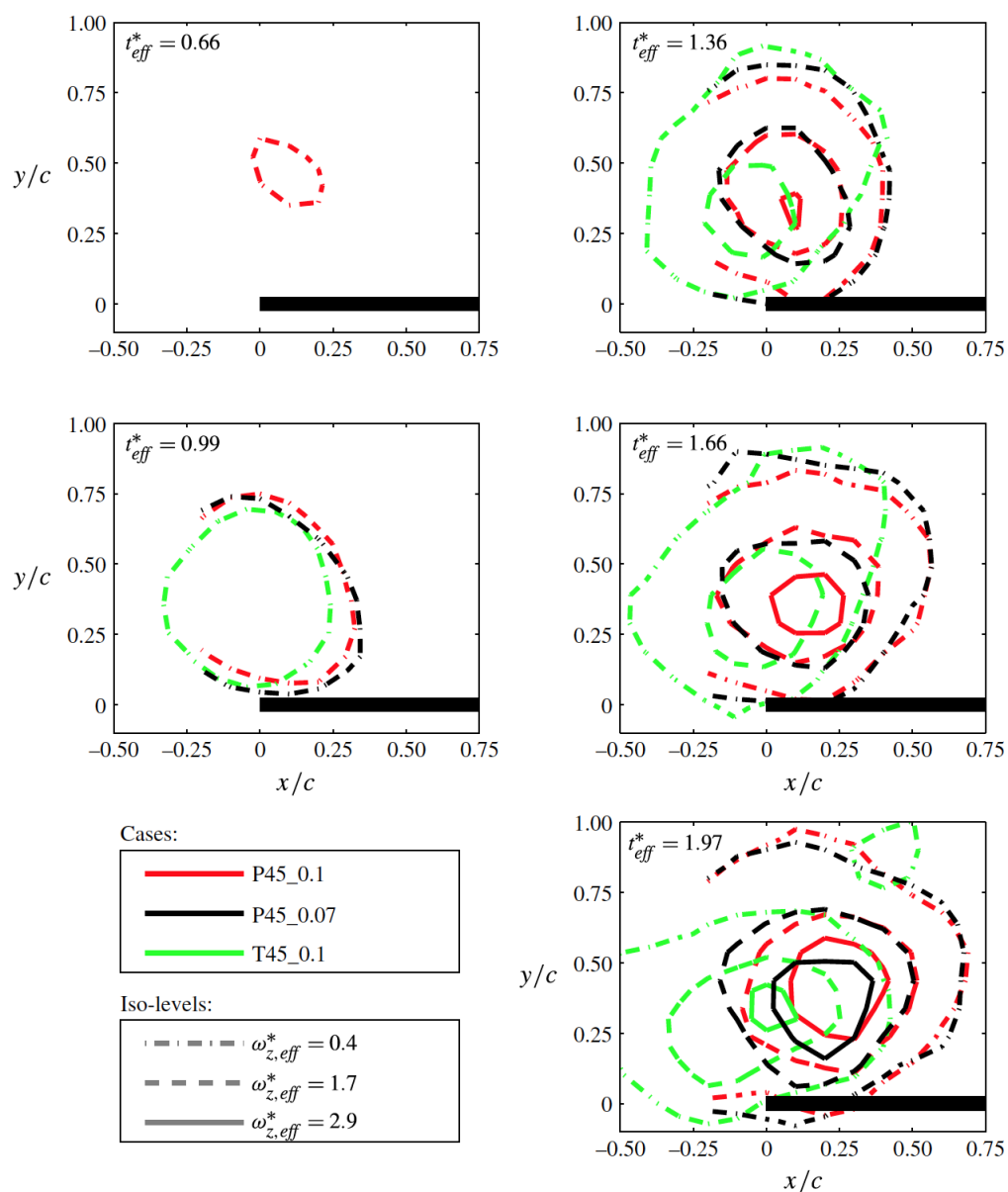
Figure 4-26: Vortex Positioning During Key Time Steps Between Plunge and Surge.

It has been demonstrated that the circulation history in the near-mid-plane region is identical for both plunging cases and T45_0.1. The corresponding total force results are shown in Figure 4-27. Here, lift and drag forces are defined to be perpendicular and parallel to the direction of the plate velocity, respectively (upper row). In addition, C_y and C_x representing the plate-normal and plate-parallel forces are plotted for comparison, respectively (lower row). All force data are non-dimensionalized based on the standard convention on the left but also using U_{eff} on the right.
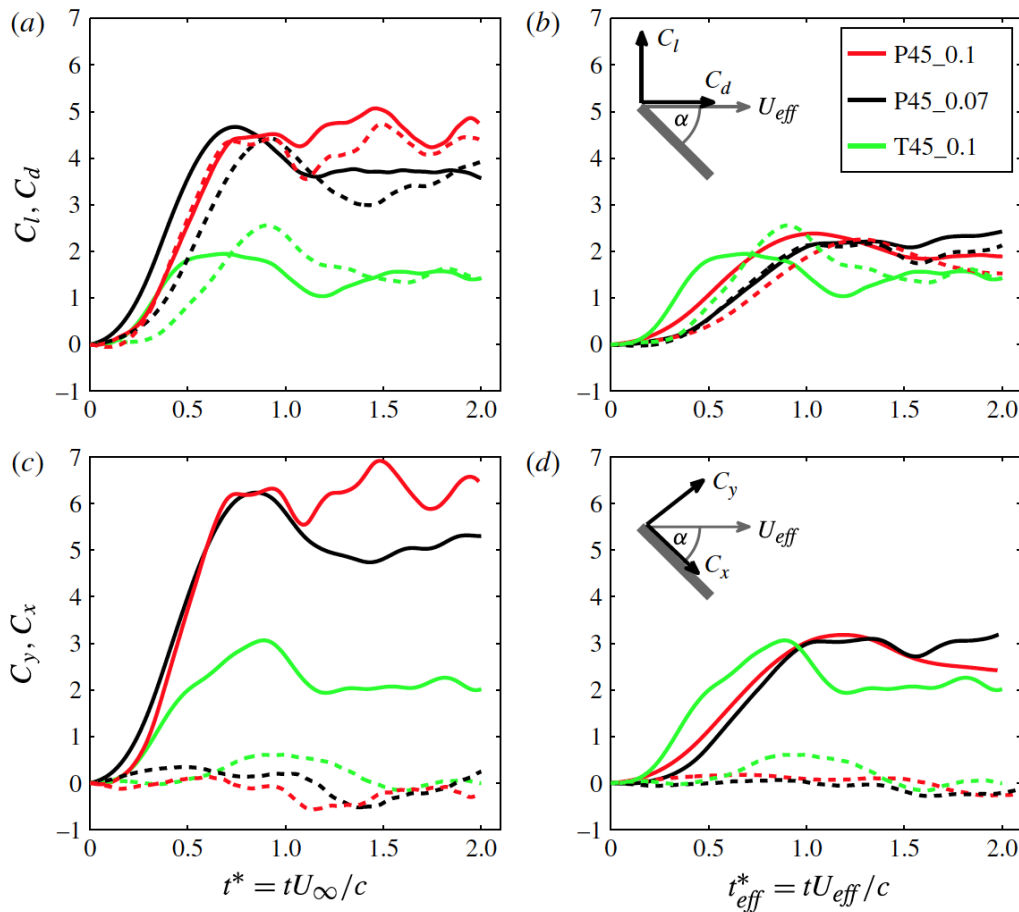
Figure 4-27: Force Coefficients Normalized on Freestream and Effective Velocities.

First, it is worth noting that the curves for the plunging motions show unexpectedly high values when normalized with the freestream velocity. In particular, the force magnitudes for T45_0.1 and P45_0.07 should be similar since the LEV is fed with the same shear-layer velocity at identical effective angles of attack. This discrepancy confirms the validity of U_{eff} as the characterizing velocity scale to describe vortex growth and thus resulting forces.

Furthermore, it is remarkable that the force histories of both plunging cases (P45_0.1 and P45_0.07) share identical curves during the plate acceleration despite the fact that they experience different magnitudes of acceleration during the respective plate motions. In contrast, the slow plunge and the tow case (P45_0.07 and T45_0.1) obviously yield significantly different force histories, even though in both cases the magnitude of plate acceleration was identical.

4.6.2 Lift and Drag for a Range of Kinematics

Here we compare four translational motions: pitch, surge, a combined "pitch-surge" and finally an "equivalent" plunge. The plunge follows rationale from the previous section, and is scaled purely by $\theta = \operatorname{atan}(\dot{h}/U_\infty)$, from which one obtains the plunge-history. This disregards the pitch pivot point effect – a crucial issue.

"Pitch-surge" begins at zero incidence with no relative free stream, and begins simultaneous increase in relative free-stream and incidence angle, both by smoothed linear ramps, until reaching the usual steady-state. The result for the 1 c motion is shown in Figure 4-28 with focus on early-time history, and in Figure 4-29 for the long-term history. Figure 4-30 covers the slow-case (6 c acceleration), where unfortunately plunge is not possible because at the low rate, the resulting vertical (plunge) displacement is not kinematically realizable in the facility where the experiment was conducted. The purely-pitching and the pitching-surging cases are again with respect to a pivot point at the leading edge (x/c = 0).
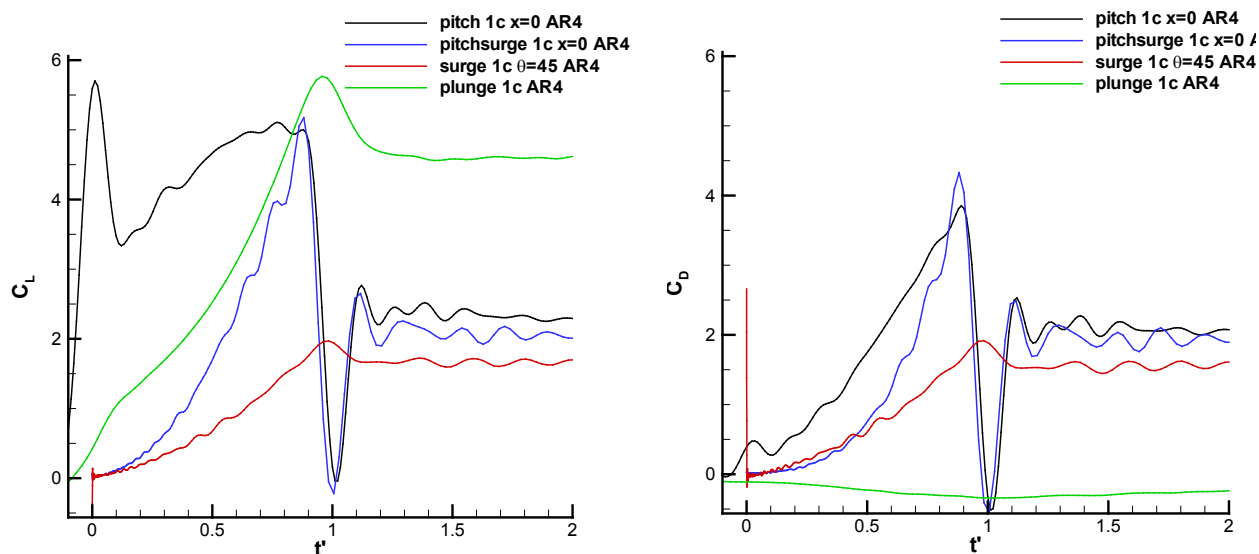
Figure 4-28: Comparison of Pitch Ramp, Pitch-Surge Ramp and Pure Surge-Ramp, 1 c Motion, AR = 4 Flat Plate; Lift (Left Column) and Drag (Right Column). Pivot point is at the leading edge (x/c = 0) for the pitch-ramp and pitch-surge ramp.
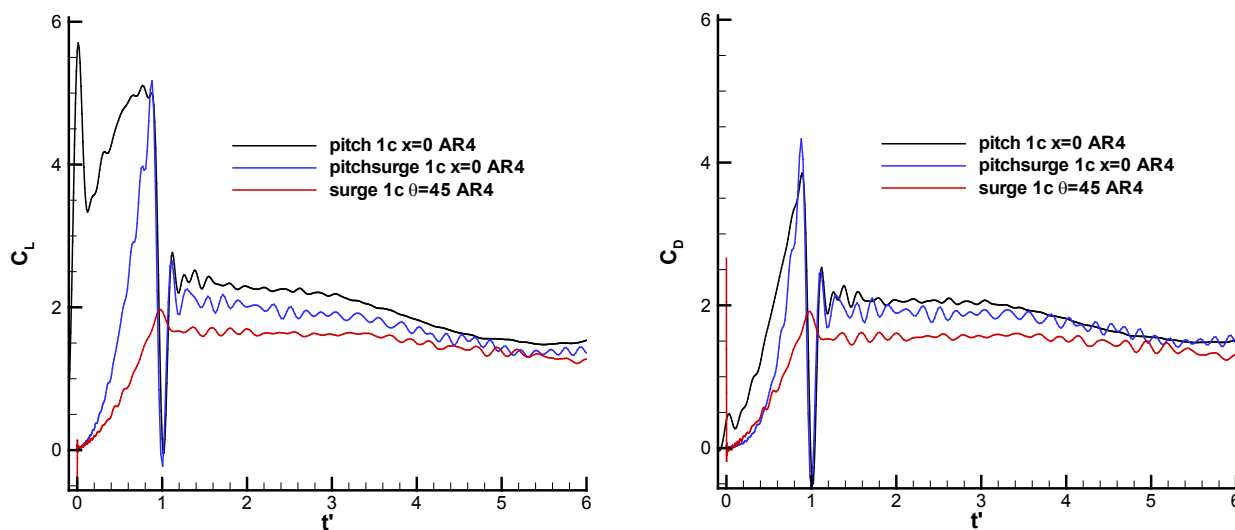
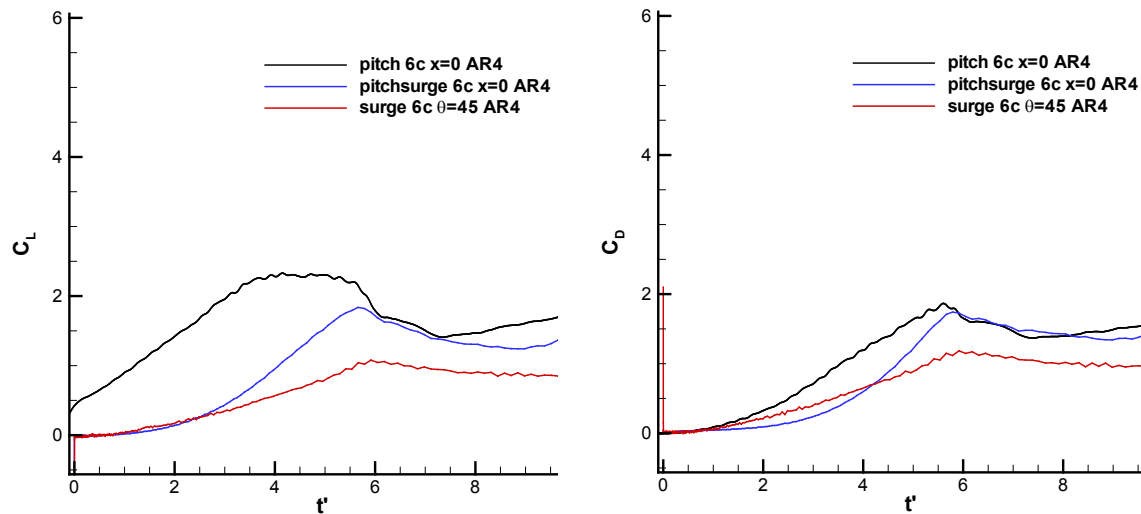**Figure 4-29: Long-Term History of Lift and Drag for AR = 4 1 c Motion Comparison.**

Figure 4-30: Comparison of Pitch Ramp, Pitch-Surge Ramp and Pure Surge-Ramp, 6 *c* Motion, AR = 4 Only; Lift (Left Column) and Drag (Right Column). Pivot point is at the leading edge (x/c = 0) for the pitch-ramp and pitch-surge ramp.

Pitch and plunge are mutually irreconcilable, owing to the aforementioned Magnus effect of pitch-rate. The pitching case has much higher lift and drag than does the respective surging case, for both motion rates. The combined pitch-surge ramp is an intermediate case, as is to have been intuitively expected. Early in the motion, (t' ~ 0), it behaves akin to the surging case, with aerodynamic force production attenuated due to low dynamic pressure. As time proceeds, the pitch-surge case comes to approximate the purely pitching case. The plunging case has a lift history somewhere in between that of the pitching and pitch-surge cases, but a drag history altogether different, with drag outright negative, evidently from strong leading edge suction. It, and the pure-surging case, completely lack a non-circulatory lift or drag spike.

4.7   VARIATIONS IN PLATE LEADING EDGE SHAPE

Here we consider the effect of using different leading and trailing edge geometries in fast and slow translational pitch, based on force measurements and PIV conducted at ITU. Because the plate is vertically suspended in a free-surface water tunnel, aerodynamically the plate is "mirrored" about the free-surface, depending on how the free-surface boundary condition is enforced: with or without an endplate, and with the plate submerged below the free-surface, or not. The following discussion, in addition to comparing the round leading edge with a squared-off or "sharp" leading edge, also considers this mirroring effect. Figure 4-31 presents lift coefficient history for the slow case, while vorticity contours, superimposed on planar projection of streamlines, are in Figure 4-32. Data in Figure 4-32 are for the AR = 4 plate, which is actually a physical aspect ratio of 2, with the mirroring effect included.
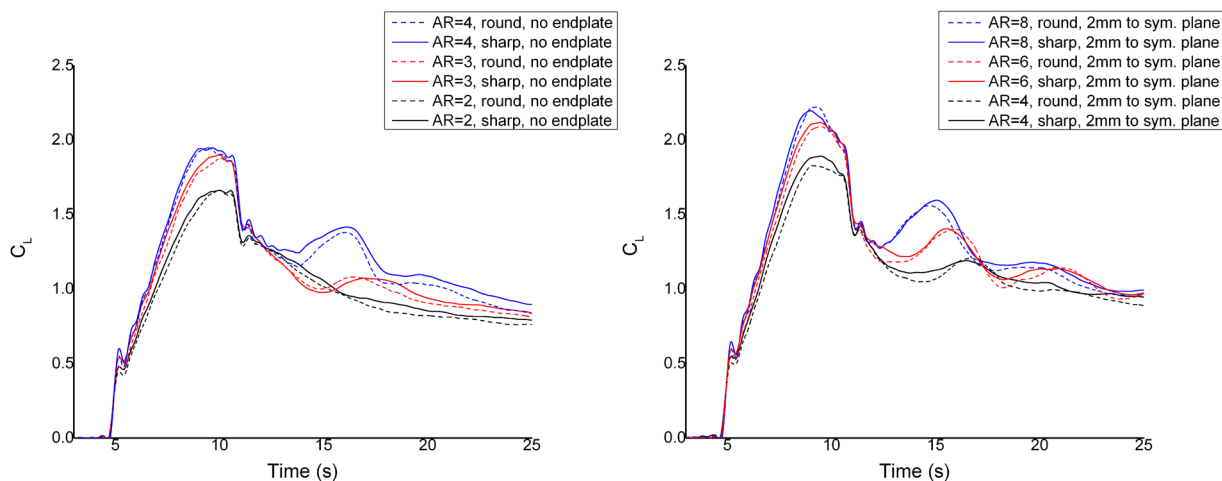
Figure 4-31: Lift Coefficient Histories for the Slow Translational Pitch Case, for Plates of Sharp and Round Leading Edge, Without (Left) and With (Right) Enforcement of a Symmetry-Plane Condition.
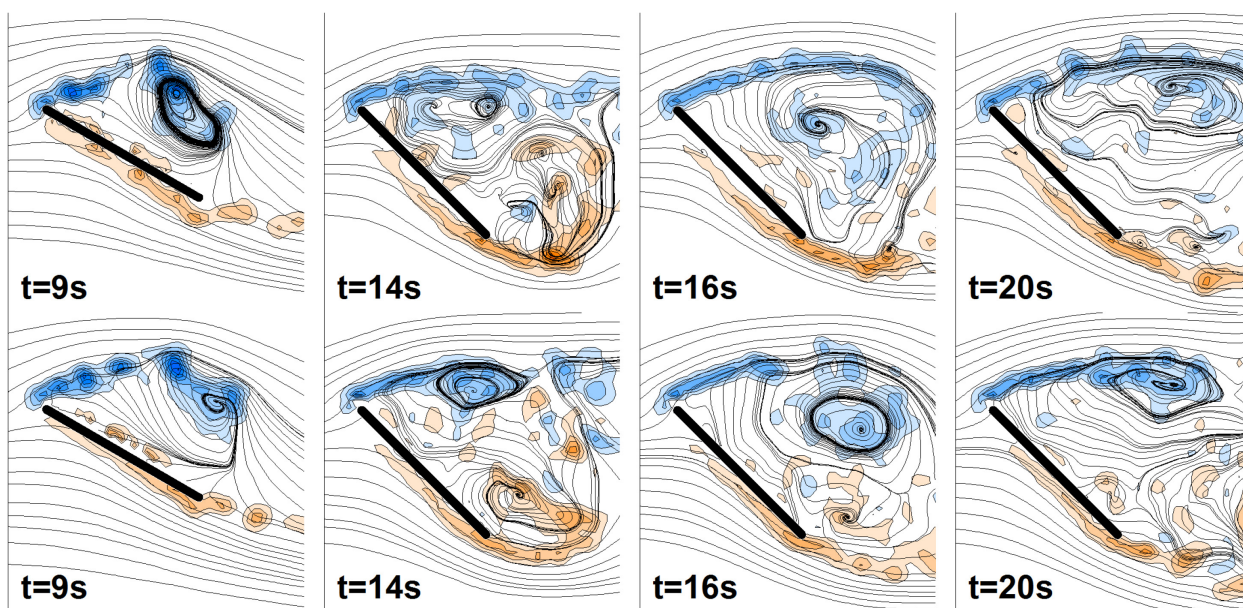

Figure 4-32: PIV Sectional Slices of Vorticity for the AR = 4 Plate: Sharp Edges (Top Row) and Round Edges (Bottom Row); Slow Translational Pitch.

Similarly, fast translational pitch lift coefficient histories are in Figure 4-33, and PIV vorticity contours and superimposed streamlines for the AR = 4 plate are in Figure 4-34. While the details of projected streamline placement are very sensitive to minor variations, overall flowfield feature evince little difference between the sharp-edge and round-edge variants of the same aspect ratio. Differences in lift coefficient history are even smaller. Evidently, leading edge shape, or edge shape in general, makes very little difference in these separated flows. Aspect ratio however does have a demonstrable effect, as already noted in a prior section.
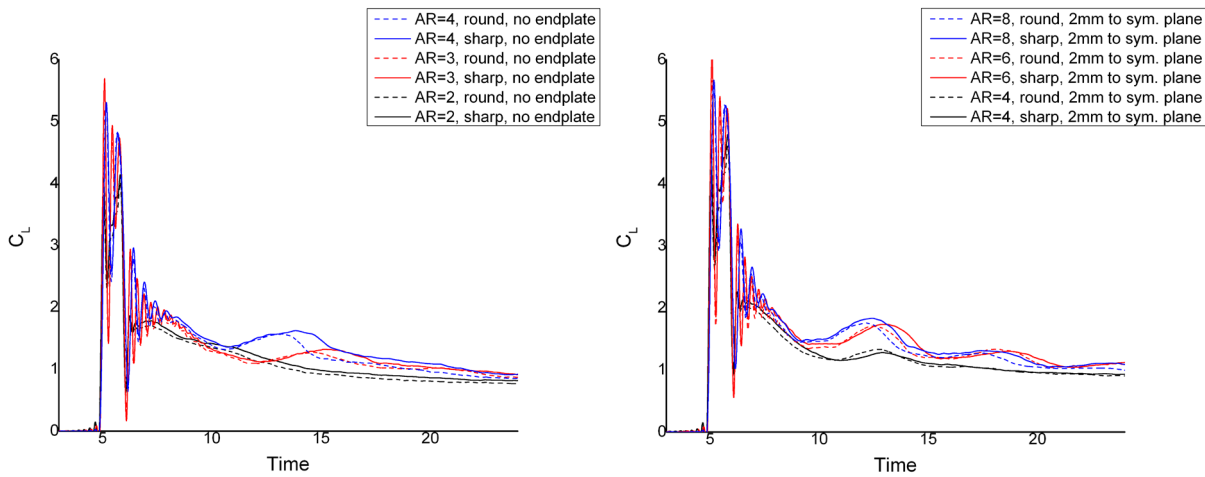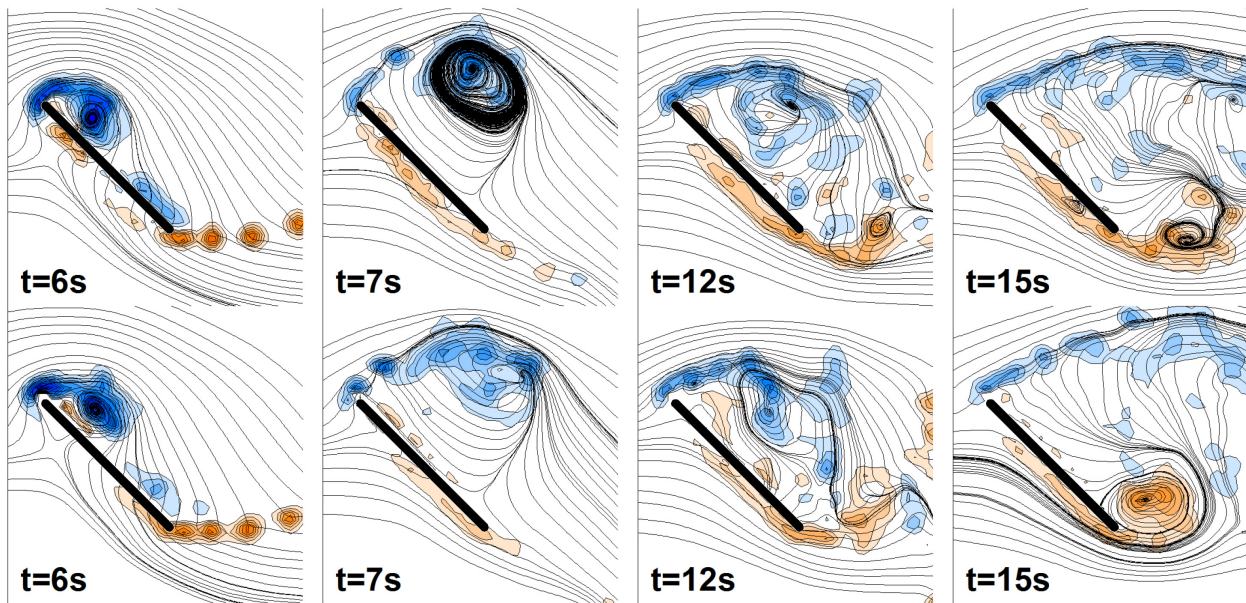
Figure 4-33: Lift Coefficient Histories for the Slow Translational Pitch Case, for Plates of Sharp and Round Leading Edge, Without (Left) and With (Right) Enforcement of a Symmetry-Plane Condition.

Figure 4-34: PIV Sectional Slices of Vorticity for the AR = 4 Plate: Sharp Edges (Top Row) and Round Edges (Bottom Row); Slow Translational Pitch.

4.8   VARIATIONS IN PEAK INCIDENCE ANGLE

Here we consider two parameter studies for the surging plate – translational and rotational, in both cases with the "fast" acceleration profile of a linear ramp over 1 c.

4.8.1 Translational Surge

Figure 4-35 covers a range of incidence angles from 5 to 90 degrees, in all cases with the same smoothed linear surge ramp over 1 c, and in all cases the respective incidence angle held constant. The low incidence case is expected to have lift coefficient follow Wagner's model [53], and for $\theta = 5\pi$ the agreement is quite good [54].
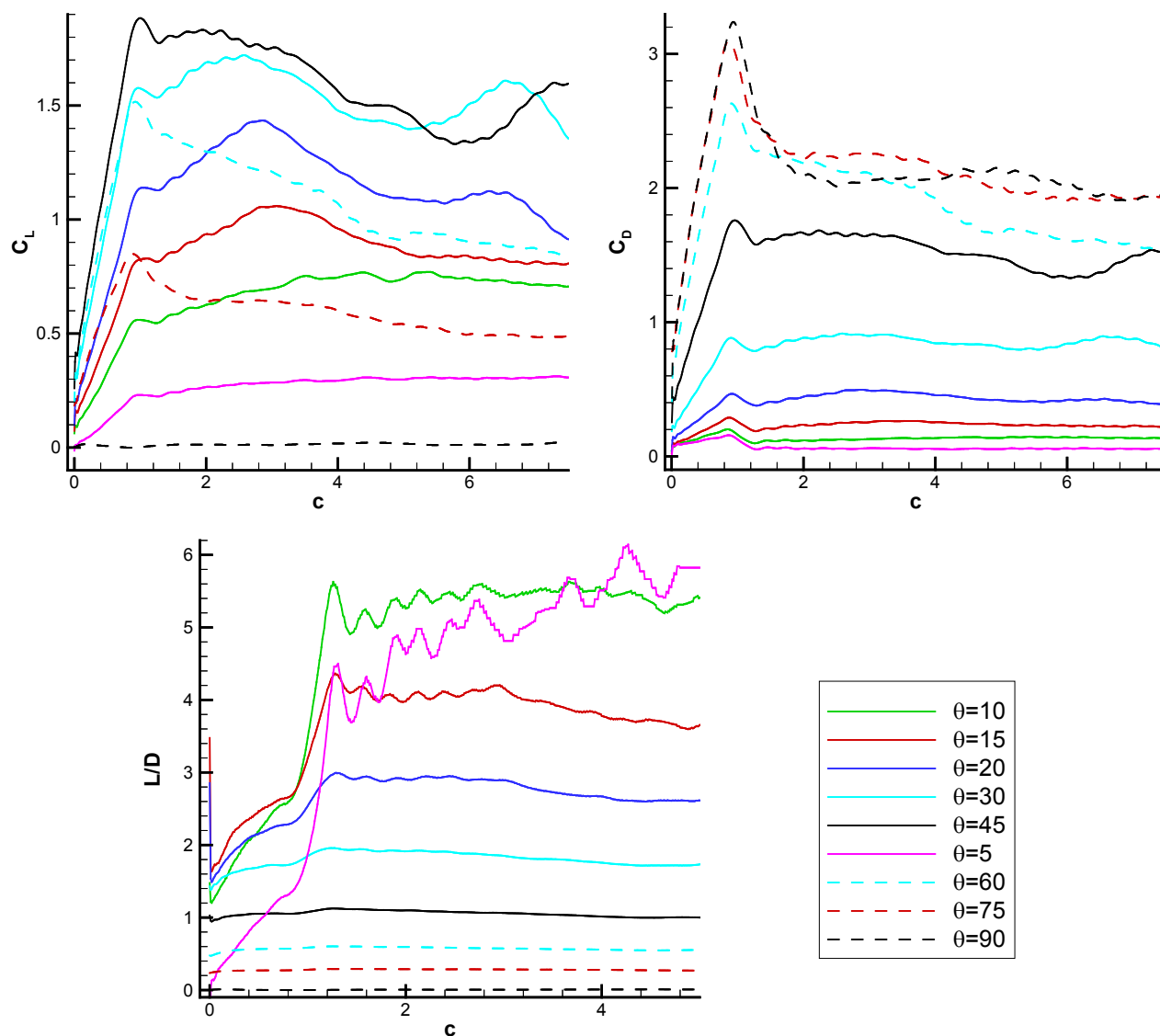

Figure 4-35: Incidence-Angle Sweep (5, 10, 15, 20, 30, 45, 60, 75 and 90 degrees) for the Fast Surging Case, Re = 20,000. Lift (top left), drag (top right), and lift-to-drag ratio (bottom). For θ = 45°, lift and drag histories essentially coincide, because the net aero force is plate-normal. For θ = 90° the lift is of course zero, and the plate acts like a piston. For all cases, peak loads are evident at the conclusion of the acceleration. The flow is separated in all cases, even (slightly) at θ = 5°; never is there any appreciable leading edge suction. However, for θ = 5°, L/D climbs after the acceleration is over, resembling a Wagner-like rise as bound circulation attains its steady-state value. For higher incidences, L/D peaks towards the conclusion of the motion. For θ = 45°, L/D ~ 1 perpetually.

4.8.2   Rotational Surge

This section covers PIV measurements for the fast rotational surging case by the TU Delft group for the AR = 2 plate, comparing incidence angles of 30 π and 60 π with the canonical case, 45 π. Flowfield data are presented as evolution vs. chords-traveled, at the radius of reference from the point of rotation. 3D iso-surfaces of Q2-criterion are shown in Figure 4-36 and Figure 4-38, while 2D contours of vorticity are shown in Figure 4-37 and Figure 4-39. Most notable is the striking qualitative similarity in flowfield between the three incidence-angle cases, and the persistence of the LEV-tip vortex pair throughout the motion history. These results are consistent with those of Wolfinger and Rockwell [16], and Garmann and Visbal [55].
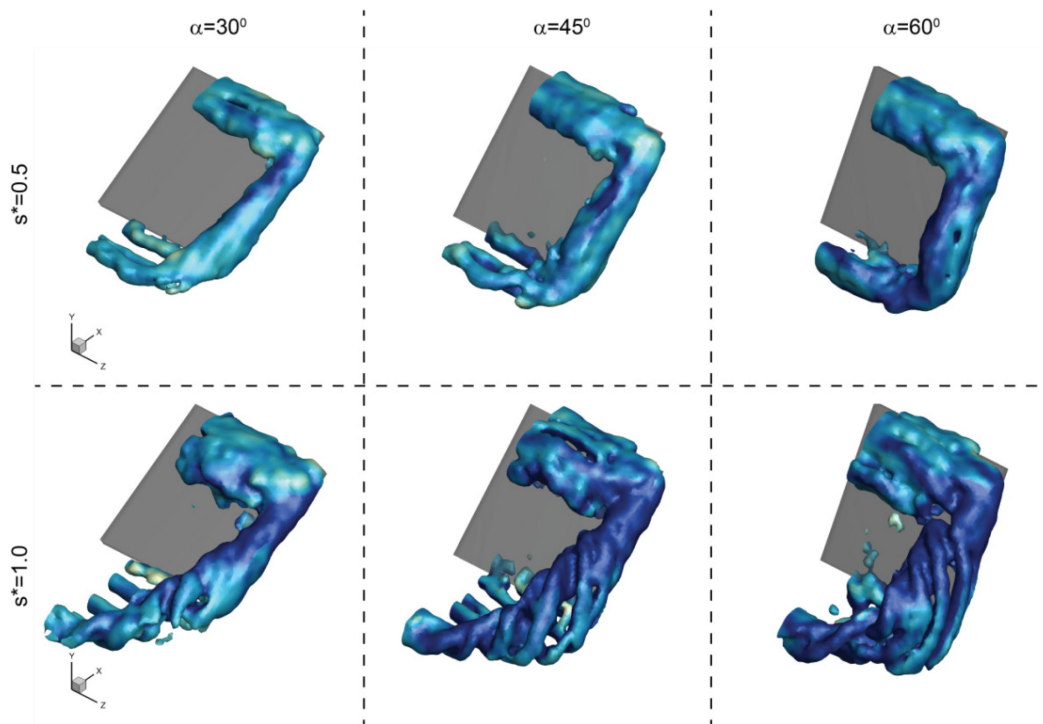

Figure 4-36: Iso-Surfaces of Normalized Q₂-Criterion, $Q/(V_t/c)^2 = 3.125$ Colored by Vorticity Magnitude; Early Time After Onset of Rotational Surge, Fast Case, Incidence Angles as Marked. Data from TU Delft Group.
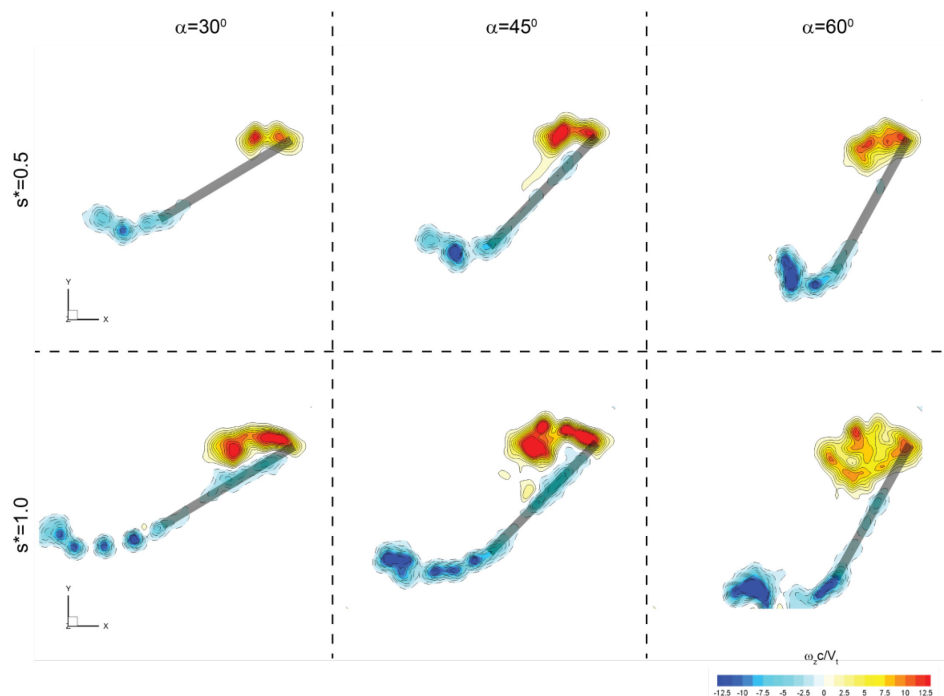
Figure 4-37: 2D Analog of Figure 4-36; Contours of Non-Dimensional Out-Of-Plane Vorticity ($\omega_z c/V_t$) in the Reference Plane, Fast Rotational Surge Case, Incidence Angles and Chords-Traveled as Marked.
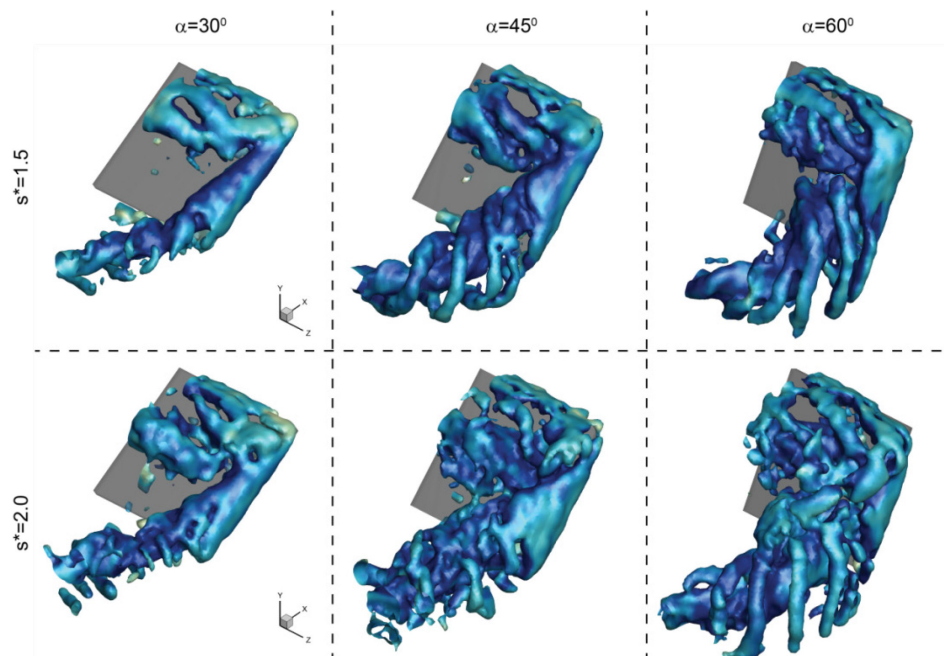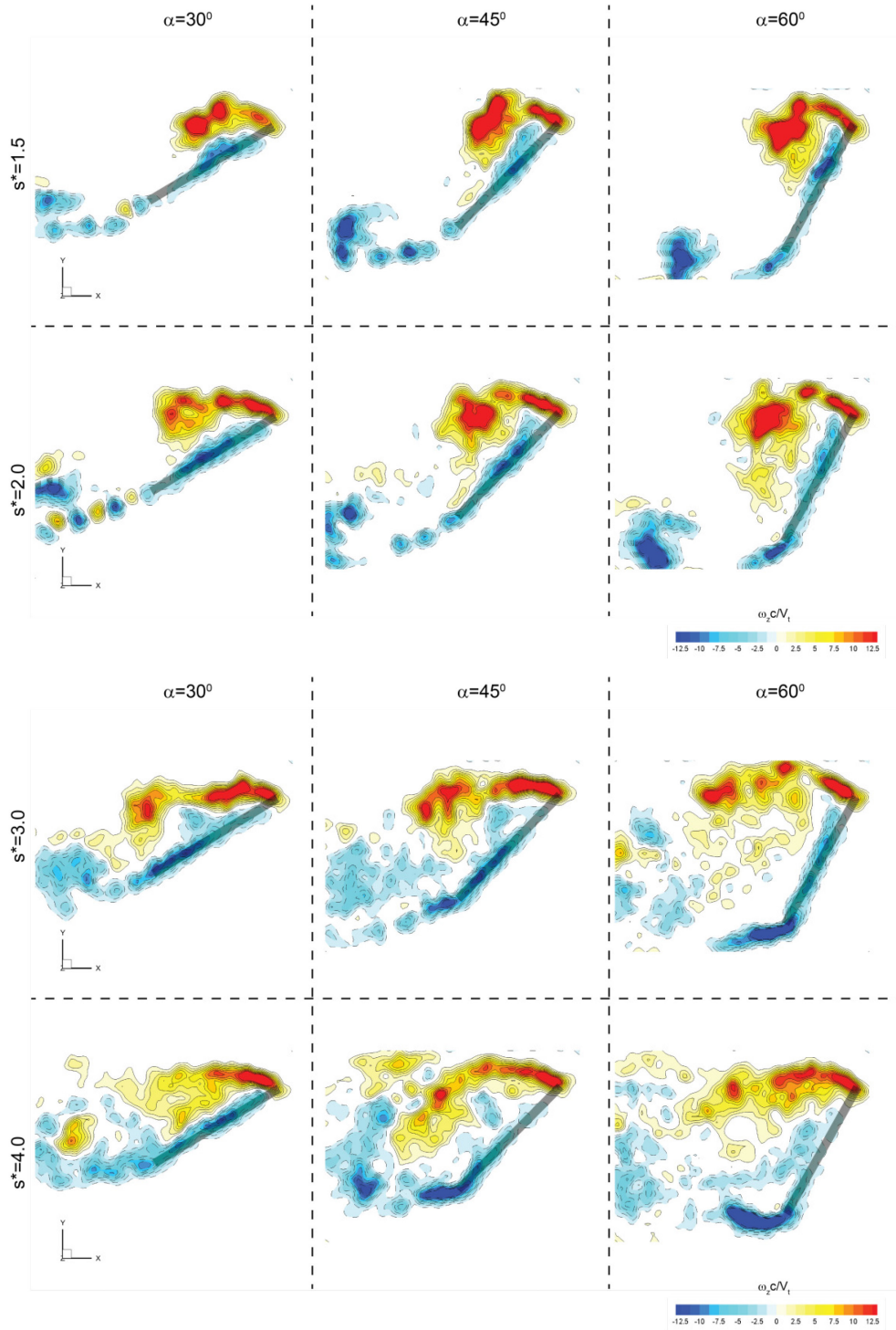

Figure 4-38: Continuation of Figure 4-36 to Later Time (that is, Later Number of Chords-Traveled at the Reference Plane); Iso-Surfaces of $Q/(V_t/c)^2 = 4.68$, Colored by Vorticity Magnitude.
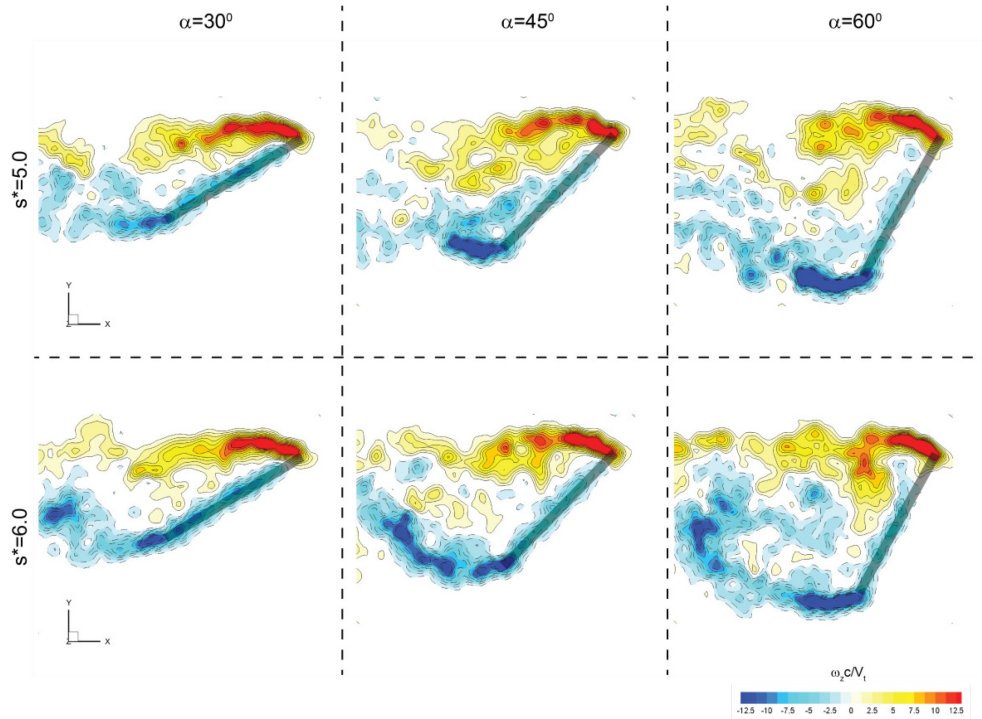
Figure 4-39: Continuation of Figure 4-37 to Later Time, Showing Essential Constancy of Flowfield Evolution Through Six Chords of Travel; Contours of Non-Dimensional Out-Of-Plane Vorticity ($\omega_z c/V_t$) in the Reference Plane.

History of lift coefficient and lift to drag ratio for fixed incidence angles of 15, 30, 45, 60 and 75 degrees is given in Figure 4-40. Peak lift to drag ratio is for the lowest incidence angle, as stands to reason given the plate-normal direction of the total aerodynamic force. This is confirmed by LD ~ 1 for the 45-degree canonical case. For all incidences there is a non-circulatory spike at motion onset, and a smoother spike towards conclusion of acceleration, followed by a gentle rise in lift to about s/c ~ 4. Thereafter aero forces settle to a more or less permanent value indicative of a stable LEV for all incidences. There is no special value of incidence angle associable with stall; all incidence angles yield more or less similar force histories and similar flowfields.
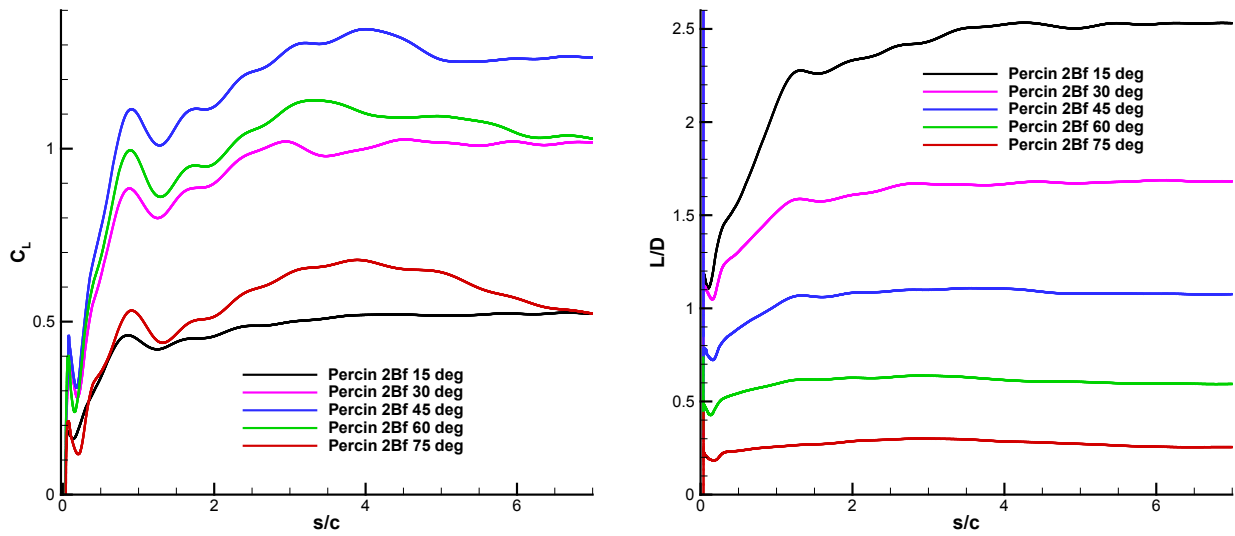
Figure 4-40: Survey of Lift Coefficient (Left) and Lift-to-Drag-Ratio (Right) Histories for "Fast" Rotational Surge, with Acceleration Occurring Over One Chord at the Reference-Plane, and Fixed Incidence Angles of 15, 30, 45, 60 and 75 Degrees. Data from TU Delft Group.